nature research

https://doi.org/10.1038/s41565-020-00788-x

Supplementary information

Permselective metal–organic framework gel membrane enables long-life cycling of rechargeable organic batteries

In the format provided by the authors and unedited

Supplementary Information

Permselective metal-organic framework-gel membrane enables long-life cycling of rechargeable organic batteries

Songyan Bai, Byunghoon Kim, Chungryeol Kim, Orapa Tamwattana, Hyeokjun Park, Jihyeon Kim, Dongwhan Lee, Kisuk Kang*

*e-mail: Kisuk Kang, matlgen1@snu.ac.kr

Supplementary Figures:

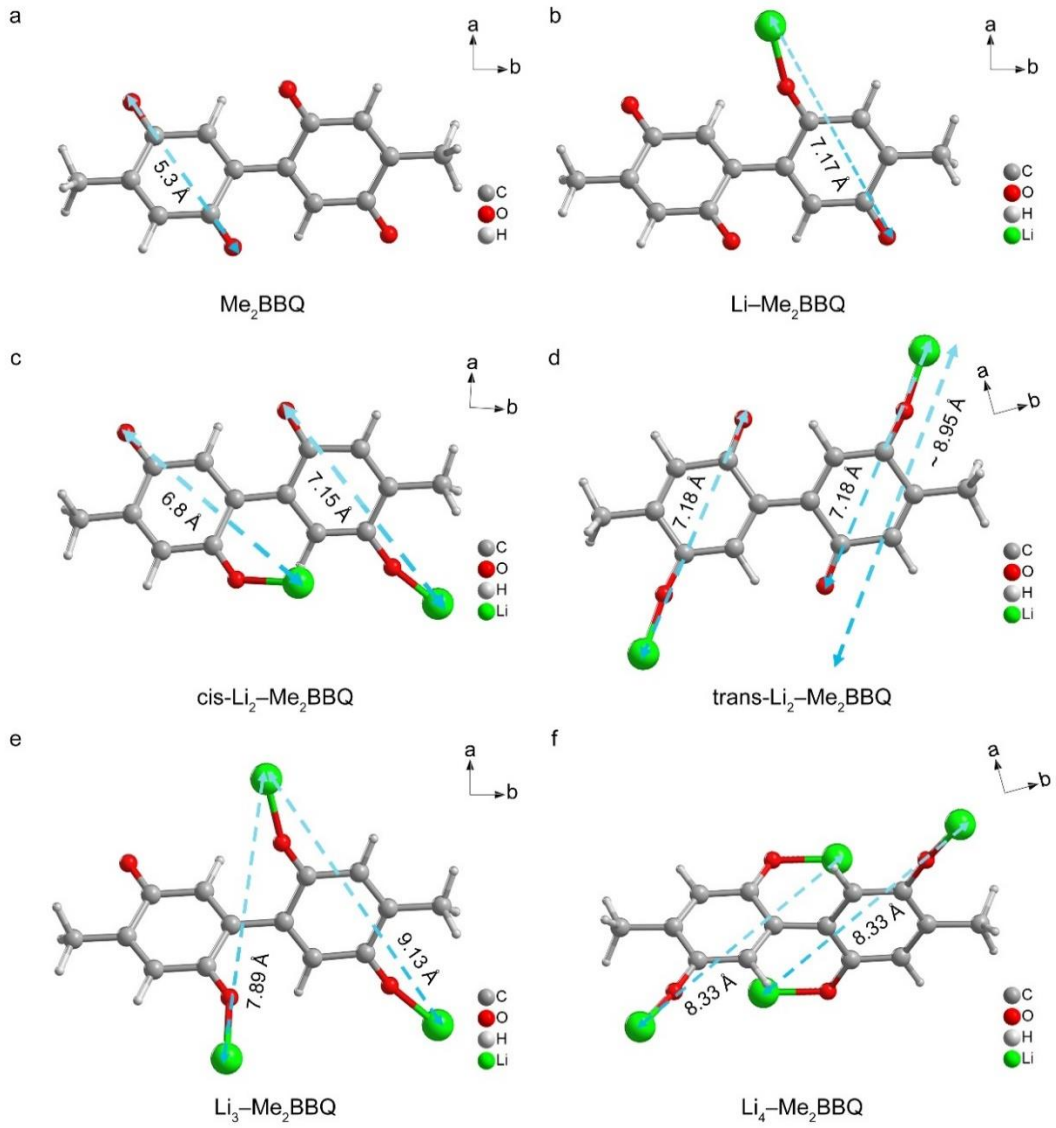

Supplementary Figure 1| The optimized structures of **a**, Me_2BBQ, **b**, Li–Me_2BBQ, **c**, cis-Li_2–Me_2BBQ, **d,** trans-Li_2–Me_2BBQ, **e,** Li_3–Me_2BBQ, and **f,** Li_4–Me_2BBQ. Geometry optimisation of the molecules was performed based on DFT calculations, as implemented in the Gaussian 09 quantum chemistry package. For Li_2-Me_2BBQ, a trans-form was calculated to be 0.21 eV more stable than a cis- form. The narrow-side width of Li_n^+–Me_2BBQ (n=1,2,3) complexes (7.15 ~ 9.13 Å) is greater than that of a single Me_2BBQ molecule (~5.4 Å). More importantly, the widths of Li_n^+ –Me_2BBQ (n=1,2,3) complexes are larger than or comparable to the channel sizes of MOF (~8.0 Å). It indicates that MOF-gel membrane is supposed to impede the permeation of Li_n^+–Me_2BBQ (n=1,2,3) complexes, while the transfer of much smaller Li^+ or solvent molecules is allowed.

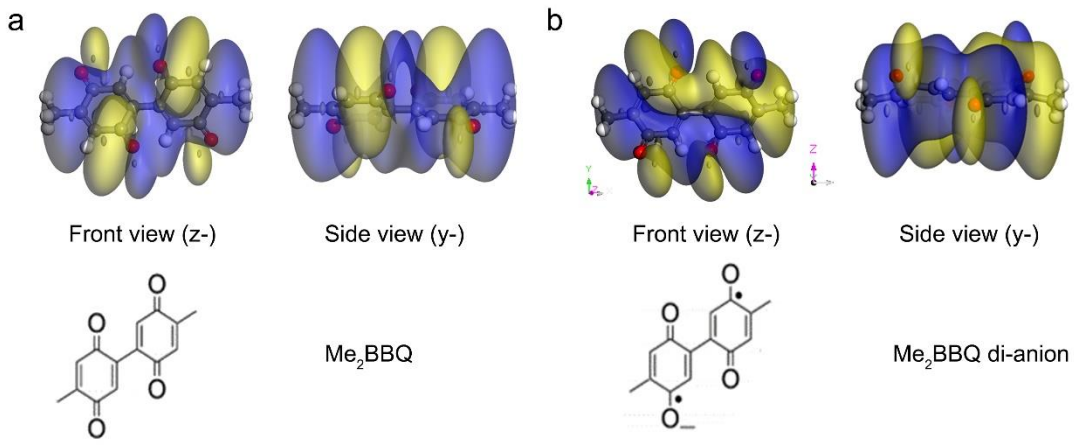

Supplementary Figure 2| The visualization of the molecular valence orbitals. **a,** Me_2BBQ **b,** Me_2BBQ di-anion intermediate. Isosurface is set to 0.003 $e^-/Å^3$.

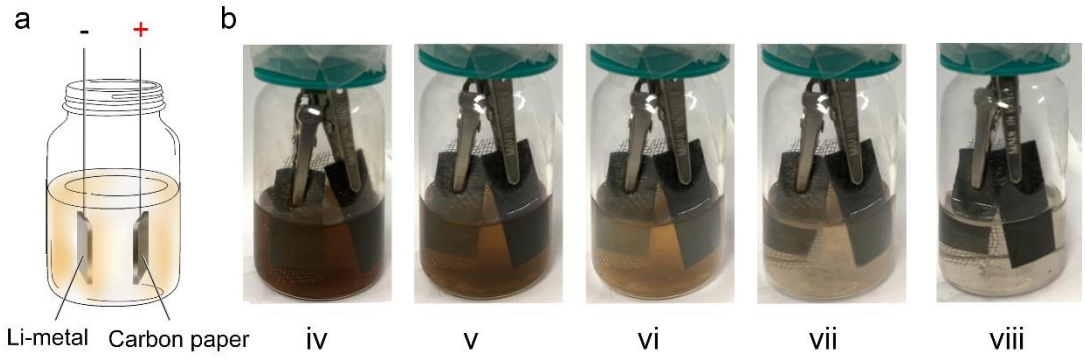

Supplementary Figure 3| a, The battery model with bare carbon paper (cathode side) and lithium metal on stainless net (anode side), **b,** The colour changes during the charge process, in which each point corresponds to points iv-viii in Figure 2. During the charge process, the dark brown solution gradually became clear and transparent. At the fully charged state, the clear solution indicates the disappearance of dissolved Me_2BBQ^{n-} complex in the electrolyte. It evidently demonstrates the solidification or recrystallization process in the electrochemical liquid-to-solid conversion.

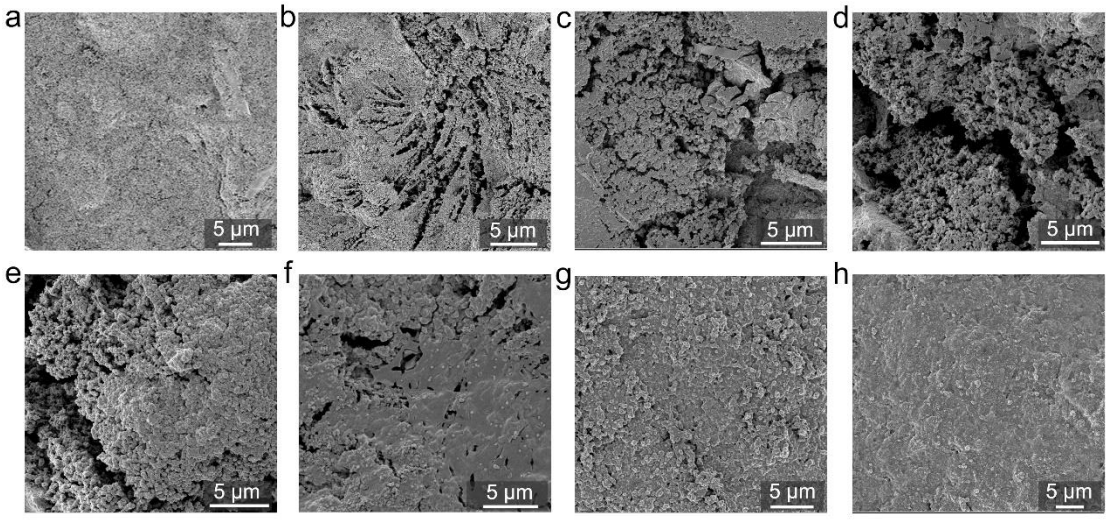

Supplementary Figure 4| Top-view surface morphologies of the Me_2BBQ electrodes at different discharge/charge states. **a,** Top-view SEM images of the pristine electrode (i points in Fig. 2a). **b-h,** Top-view SEM images of the organic electrode corresponding to ii-viii points in Fig. 2a.

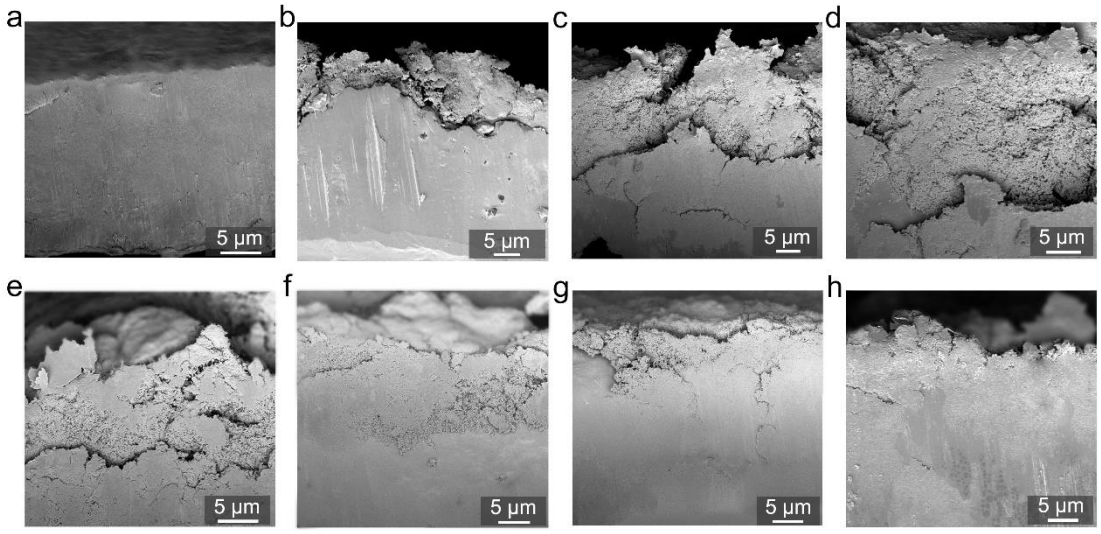

Supplementary Figure 5| Cross-section surface morphologies of the Me_2BBQ electrodes at different discharge/charge states. a, Cross-section SEM images of the pristine electrode (i points in Fig. 2a). **b-h,** Cross-section SEM images of the organic electrode corresponding to ii-viii points in Fig. 2a.

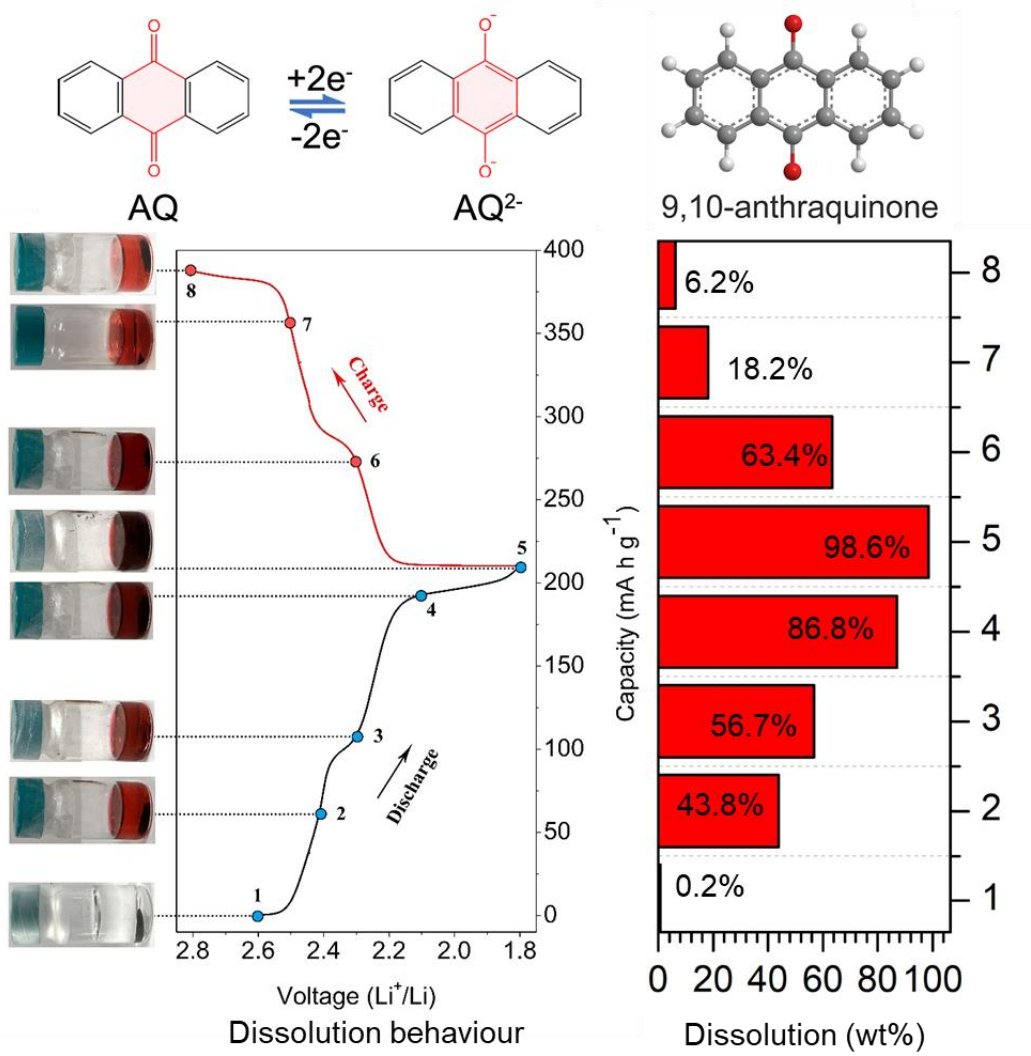

Supplementary Figure 6| Dissolution behaviour of 9,10-anthraquinone (abbreviated as 9,10-AQ) in Li-AQ battery. There are ~ 99wt% of 9,10-AQ dissolved in electrolyte at the full discharge stage.

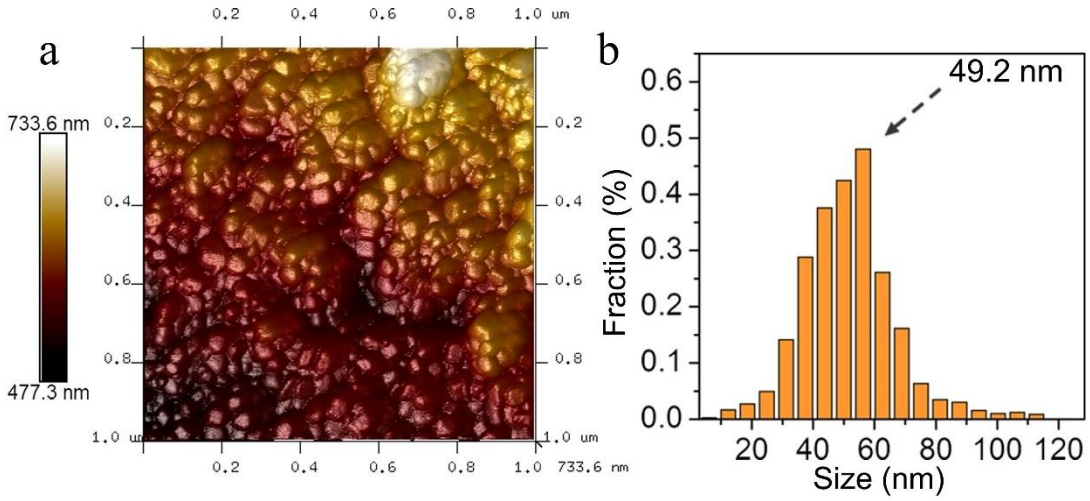

Supplementary Figure 7| AFM analysis of the ZIF-8 gel separator. **a,** Root mean square roughness (Rq):14.0 nm. Arithmetic average roughness (Ra):11.1 nm. Scale bar, 1 μm. **b,** Grain size distribution observed by AFM data.

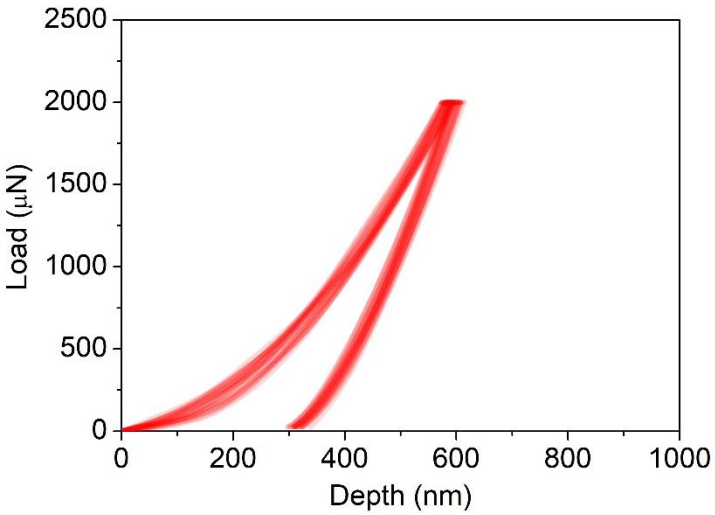

Supplementary Figure 8| The load–displacement test of MOF-gel separator. 100 indents were performed using 600nm penetration depths.

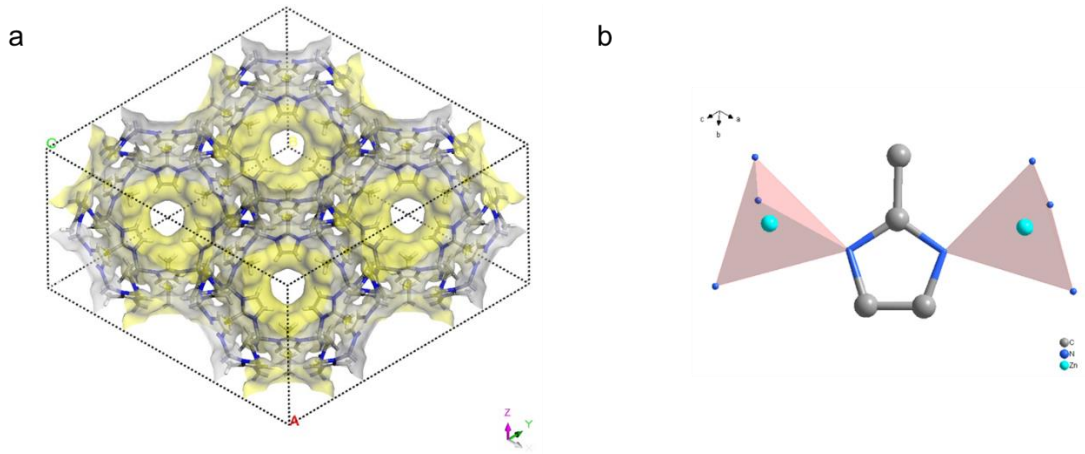

Supplementary Figure 9| Schematic showing **a,** the porous structures and **b,** coordination of the Zeolitic Imidazolate Framework (ZIF-8). The zinc ions are joined by bridging 2-methylimidazole rings.

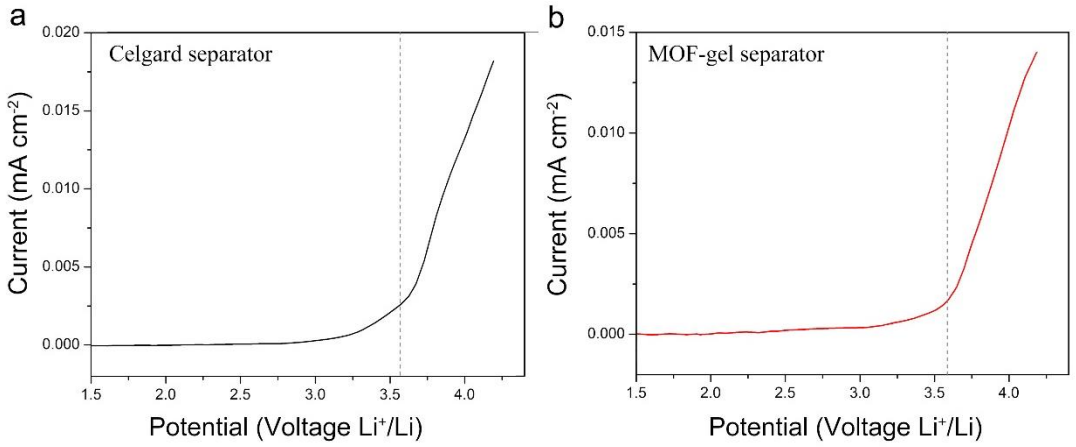

Supplementary Figure 10| Linear sweep voltammogram for **a,** MOF-gel separator **b,** Celgard separator between 1.5 V to 4.2 V with a scanning rate of 1 mV s^{-1}.

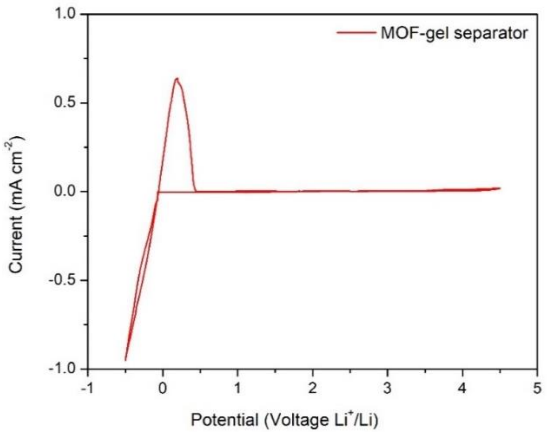

Supplementary Figure 11| Cyclic voltammetry for MOF-gel separator between -0.5 V to 4.5 V with a scanning rate of 1 mV s^{-1}.

Supplementary Figure 12| Immersing the MOF-gel separator in electrolyte over 6 months. It retained stable morphologies in electrolyte.

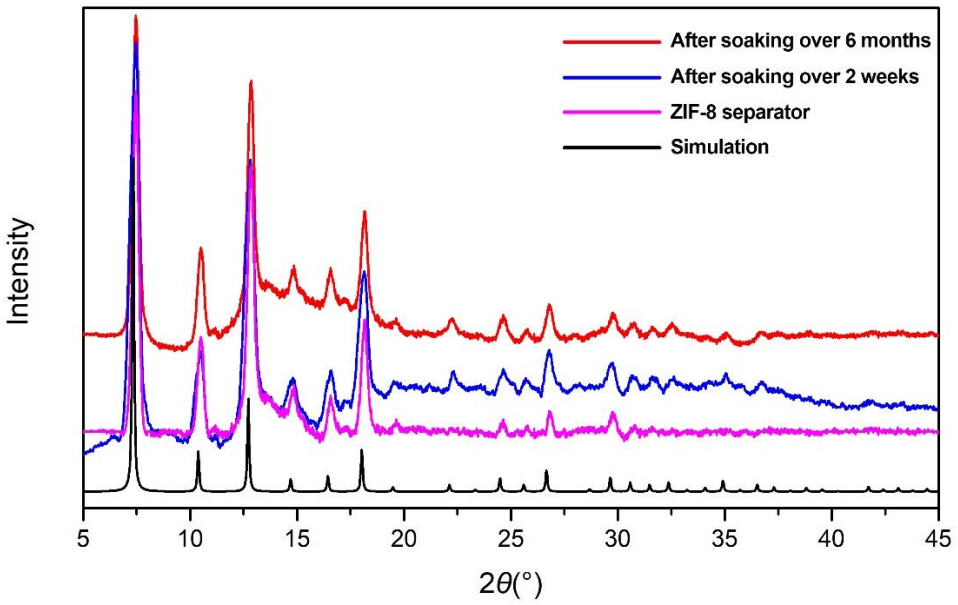

Supplementary Figure 13| The well-matched PXRD peaks of MOF-gel separator when soaking in electrolyte over 6 months.

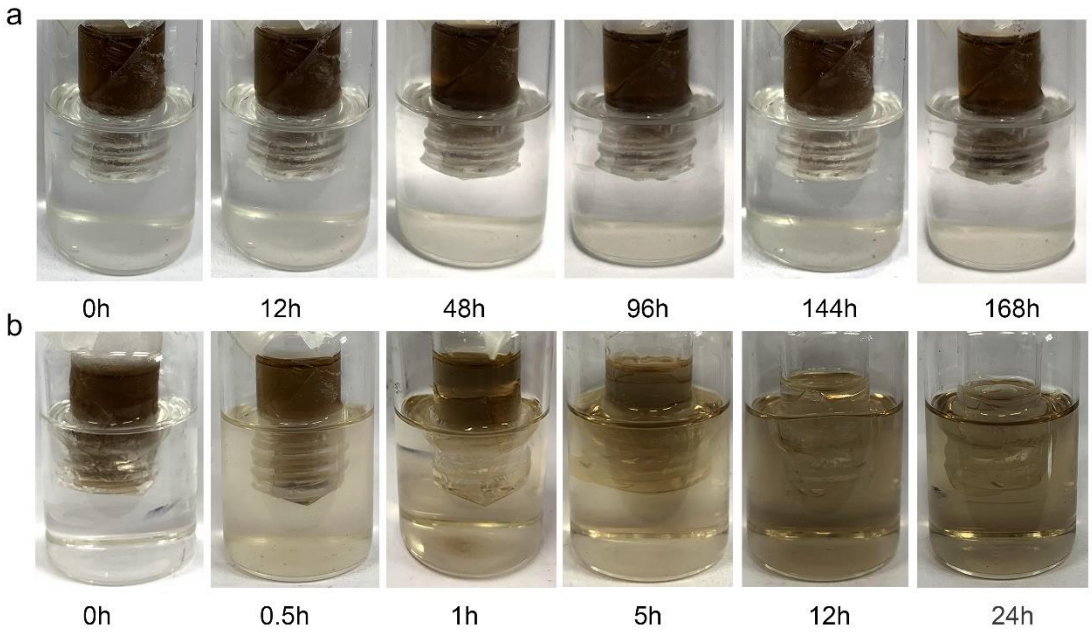

Supplementary Figure 14 | Permeation measurements. a, Inner–outer cylinder device with a MOF-gel separator. The brown redox intermediates can scarcely pass through the MOF-gel separator over 168 h. **b,** Inner–outer cylinder device with a conventional Celgard separator. Obvious colour changes were observed in the outer cylinder. The organic redox intermediates gradually permeated through the conventional separator and occupied the outer cylinder within 24 h.

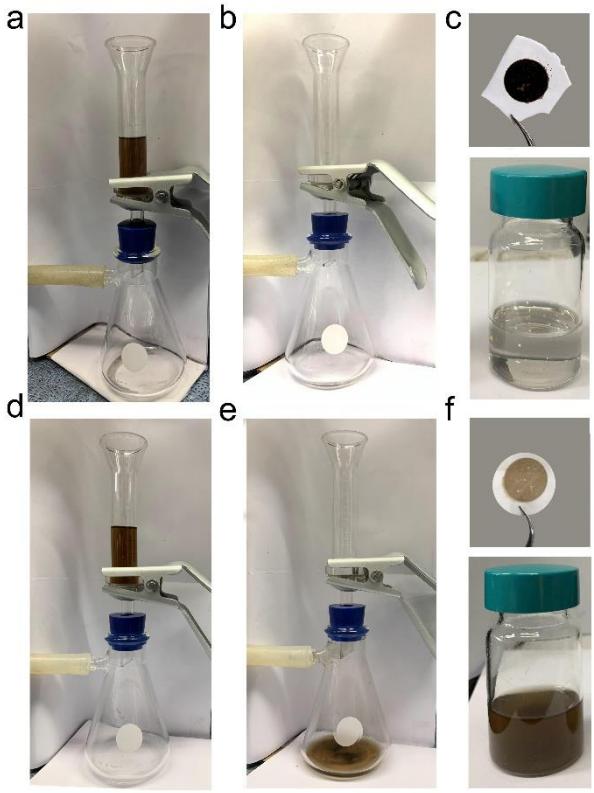

Supplementary Figure 15| The filtration experiments with **a-c,** MOF-gel separator and **d-f,** conventional separator (Whatman® PVDF membrane, pore size: 0.2 μm). Before the filtration, the dark brown solution (10 ml) of the dissolved Me_2BBQ^{n-} was placed on the upper bottle of the device, which was separated from the bottom flask by each separator. In **a-c,** the transparent solution on the bottom after filtration suggests the highly efficient sieving effect of MOF-gel separator. The black stains were observed to be accumulated on top of the MOF-gel separator, which evidently suggests that Me_2BBQ^{n-} redox intermediates could be filtered out. In contrast, the dark brown coloured solution simply passed through the conventional separator upon the vacuum filtration, leaving a trace of the stains on the separator as shown in **d-f**. It indicates that unlike the conventional separator, the self-assembled MOF-gel separator could function as a permselective membrane for Me_2BBQ^{n-} redox intermediates.

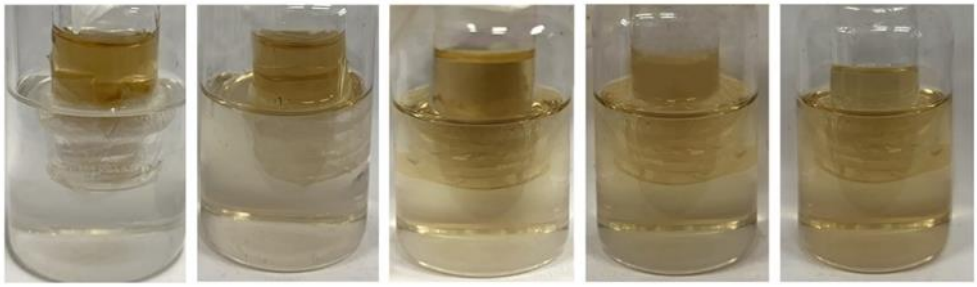

Supplementary Figure 16| Inner-outer cylinder device with a MOF-gel separator. The golden-coloured solution was prepared by immersing fully discharged *p*-benzenquinone (BQ) electrode into the electrolyte over one night. Considering that the soluble BQ^{2-} redox intermediates are smaller than the channel size of ZIF-8 species, the golden-coloured BQ^{2-} redox intermediates in the inner cylinder solution diffused out through the MOF-gel separator, gradually changing the colour of the outer-cylinder blank electrolyte. The colour of the blank electrolyte began to change after 2 hours; thus, the permeation appeared to be slightly slower than for the conventional separator. The colour of the outer-cylinder solution continued to change until it became nearly golden after 36 hours. The permeation of the soluble BQ^{2-} redox intermediates through the MOF-gel separator was further validated by the UV-vis spectra in Supplementary Fig. 17.

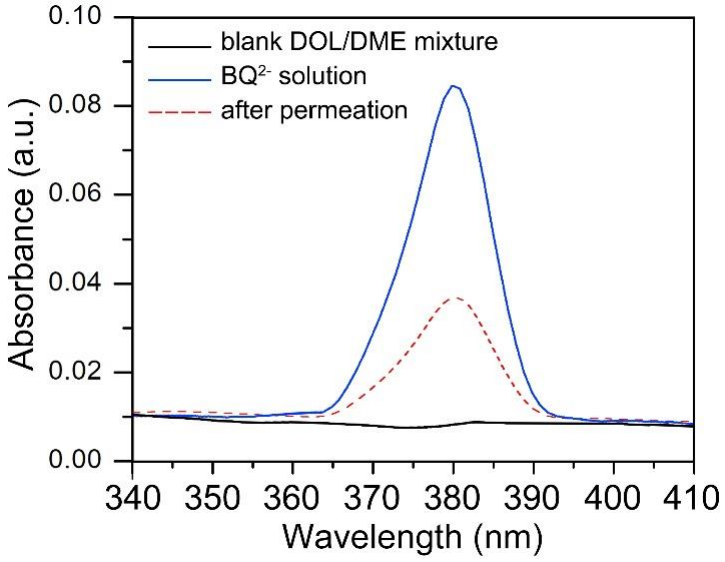

Supplementary Figure 17| The UV-Vis spectra in permeation experiments. Blank DOL/DME mixture (Black) and BQ^{2-} solution before the permeation experiments (Blue) and after the permeation experiments (Red) are shown. The characteristic peak of the BQ^{2-} redox intermediates at ~380 nm, which did not appear for the blank electrolyte, significantly grew in intensity after the permeation experiment, confirming the pass-through of the BQ^{2-} intermediates.

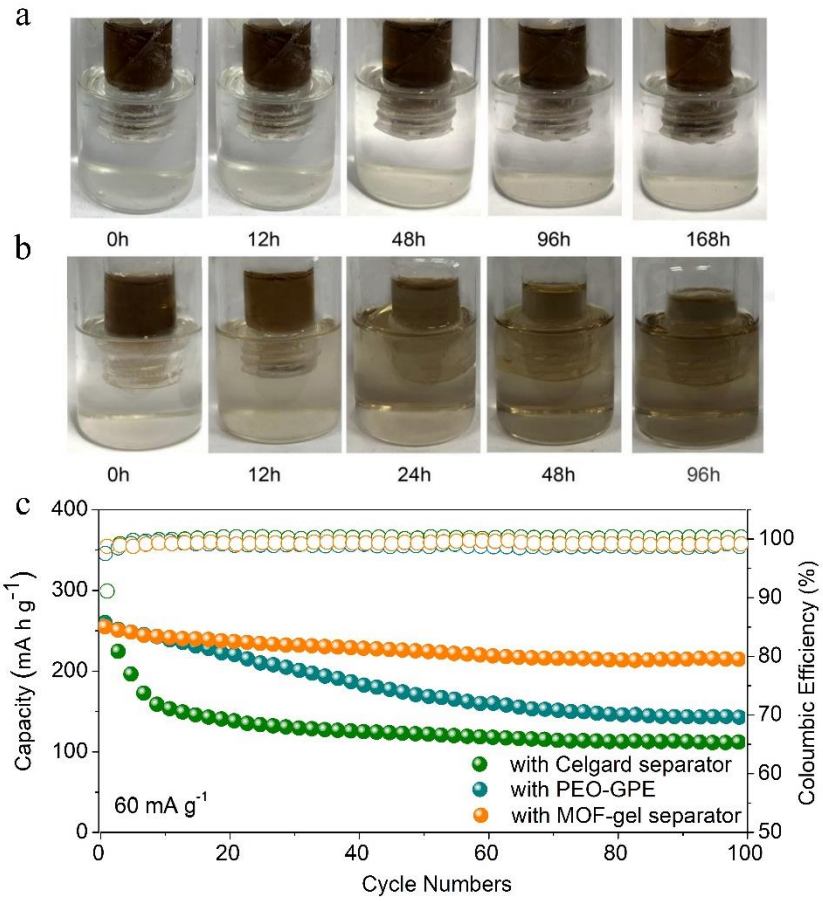

Supplementary Figure 18 | Comparison of the sieving capability of the MOF-gel separator and PEO-gel separator. a, Inner–outer cylinder device with a MOF-gel separator. The brown redox intermediates can scarcely pass through the MOF-gel separator over 168 h. **b,** Inner–outer cylinder device with PEO-GPE. Obvious colour changes were observed in the outer cylinder. The organic redox intermediates gradually permeated through the conventional separator and occupied the outer cylinder within 96 h. **c,** Electrochemical performance of Li–Me_2BBQ batteries with Celgard separator (Green), PEO-GPE (Cyan) or MOF-gel separator (Orange). All data was obtained at current density of 60 mA g^{-1} over 100 cycles. The sieving capability of MOF-gel separator comes from the homogeneous micropores in MOF structures which can act as selective channels for targeted organic intermediates. By tuning the channel size of MOF, we can allow or prohibit the passage toward specific molecular targets.

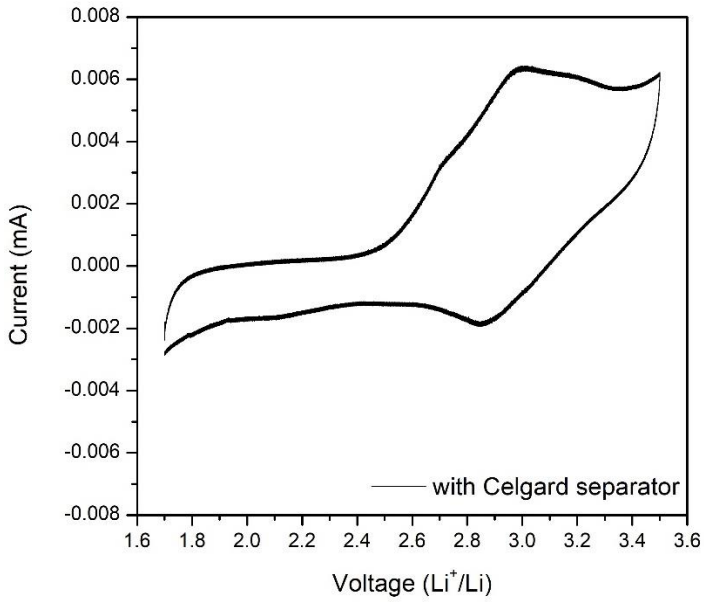

Supplementary Figure 19| The CV spectrum of Li–Me_2BBQ battery with Celgard separator at 0.1 mV s^{-1}.

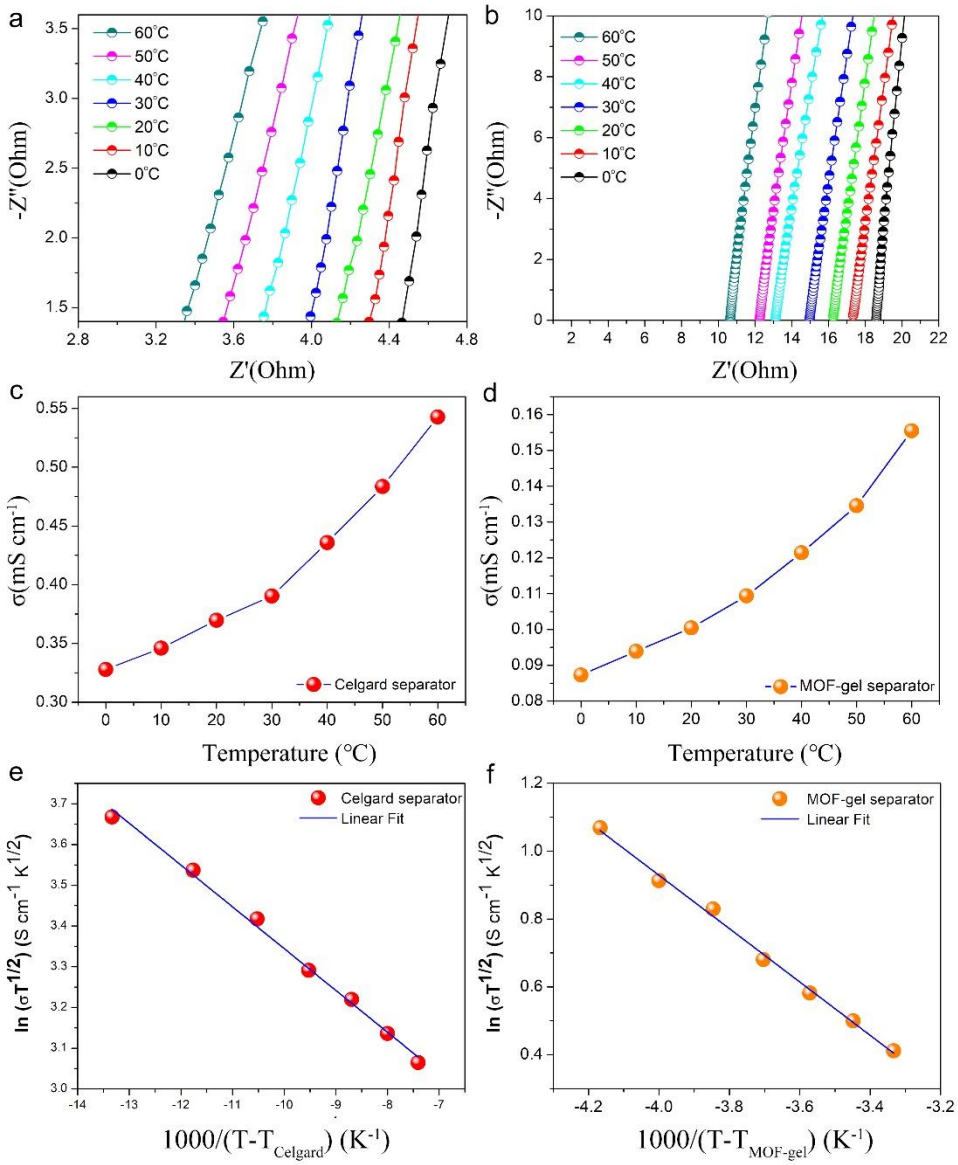

Supplementary Figure 20| Impedance spectra and corresponding ion conductivity of **a, c,** the Celgard separator and **b, d,** MOF-gel separator. At ambient temperature, Li^+ ionic conductivity of Celgard separator and MOF-gel separator is 0.38 mS cm^{-1} and 0.1 mS cm^{-1}, respectively. The linear fits of the activation energy of **e,** the Celgard separator and **f,** MOF-gel separator. At ambient temperature, activation energy for Li^+ conduction was calculated to be 0.1 and 0.78 eV for Celgard separator and MOF-gel separator, respectively.

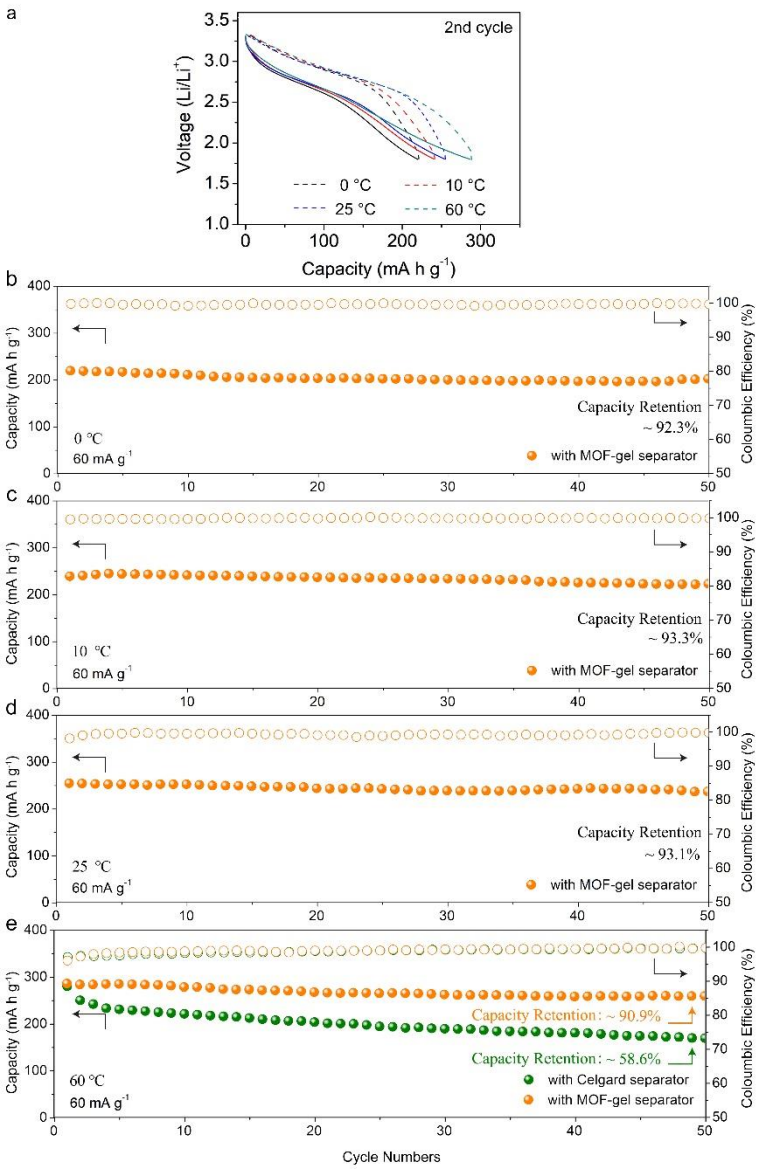

Supplementary Figure 21| **a**, The second cycle voltage profiles of Li–Me_2BBQ batteries with MOF-gel separators at various temperatures. **b-e**, Cycling performance of Li–Me_2BBQ batteries at **b,** 0 ℃, **c,** 10 ℃, **d,** 25 ℃, and **e,** 60 ℃, respectively. Cycling performance of Li–Me_2BBQ batteries with the MOF-gel separator and conventional Celgard separator at **e,** 60 ℃.

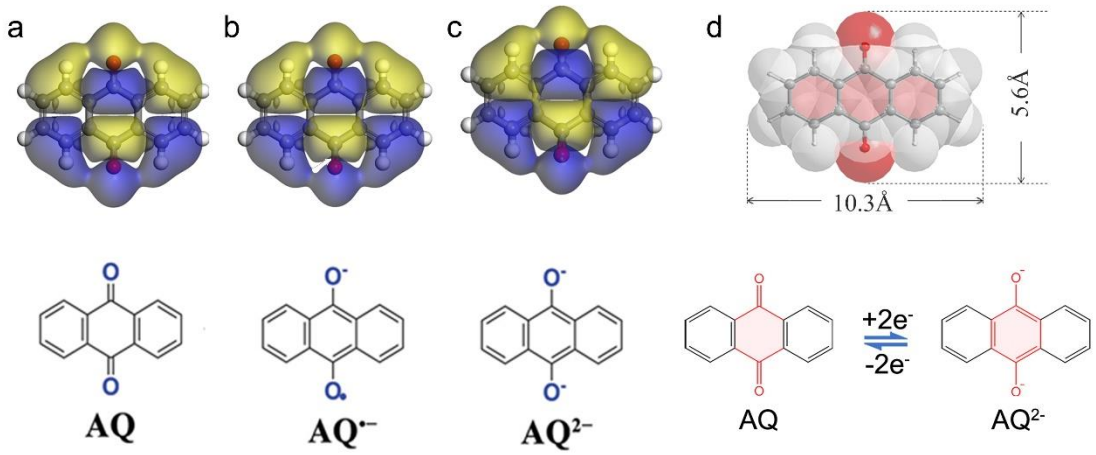

Supplementary Figure 22| The visualization of molecular valence orbitals of **a,** AQ, **b,** $AQ^{\bullet-}$ and **c,** AQ^{2-} intermediates. Isosurface is set to 0.003 $e^-/Å^3$. The available migration path of ZIF-8 is ca. 8Å of width, smaller than the length of serial AQ^{n-}(n=1,2) redox intermediates (~10.3 Å), while it remains sufficiently big for the permeability of other salts and solvents in the electrolyte.

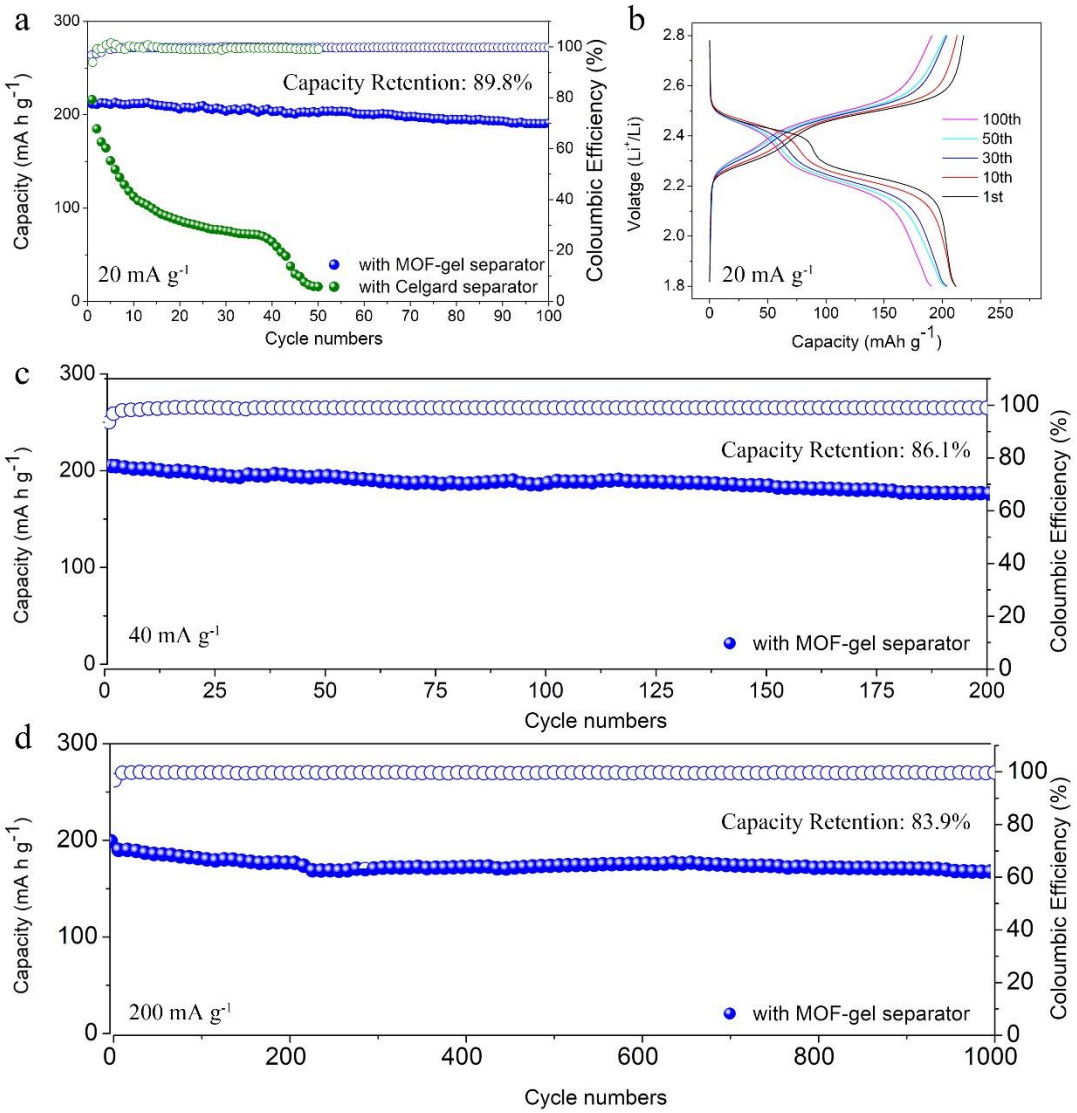

Supplementary Figure 23| Electrochemical performance of the Li–AQ batteries. Comparison of the batteries with Celgard separator or MOF-gel one at the current densities of 20 mA g^{-1}, 40 mA g^{-1} and 200 mA g^{-1} at the areal mass loading of 2 mg cm^{-2}.

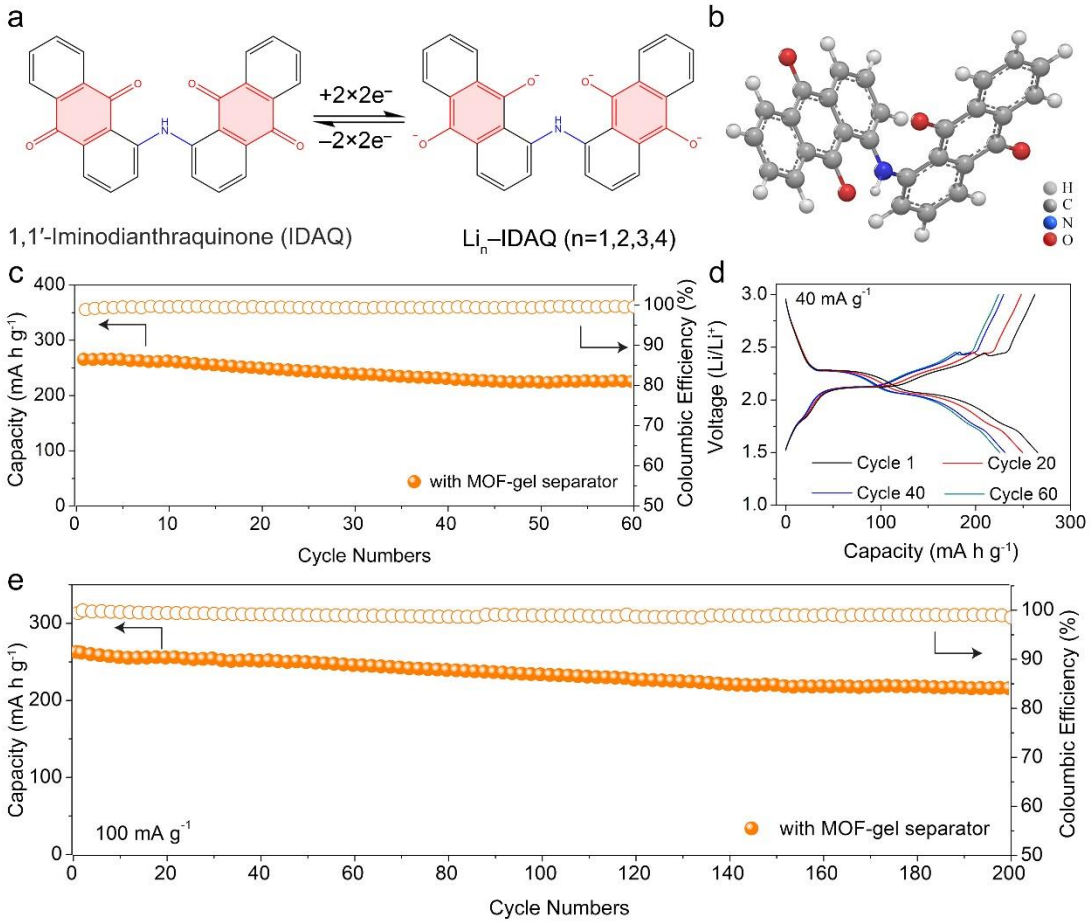

Supplementary Figure 24 | Electrochemical performance of Li-IDAQ batteries. a, The proposed electrochemical redox reaction. **b,** The structures of Li_4-IDAQ intermediates. **c,** Cycling performance and coulombic efficiency for a current density of 40 mA g^{-1} for 60 cycles with MOF-gel separator. The capacity retention was 91% after 60 cycles. **d,** Discharge/charge voltage profiles at a current density of 40 mA g^{-1} with MOF-gel separator. **e,** Extended cycling performance and coulombic efficiency at a current density of 100 mA g^{-1} over 200 cycles.

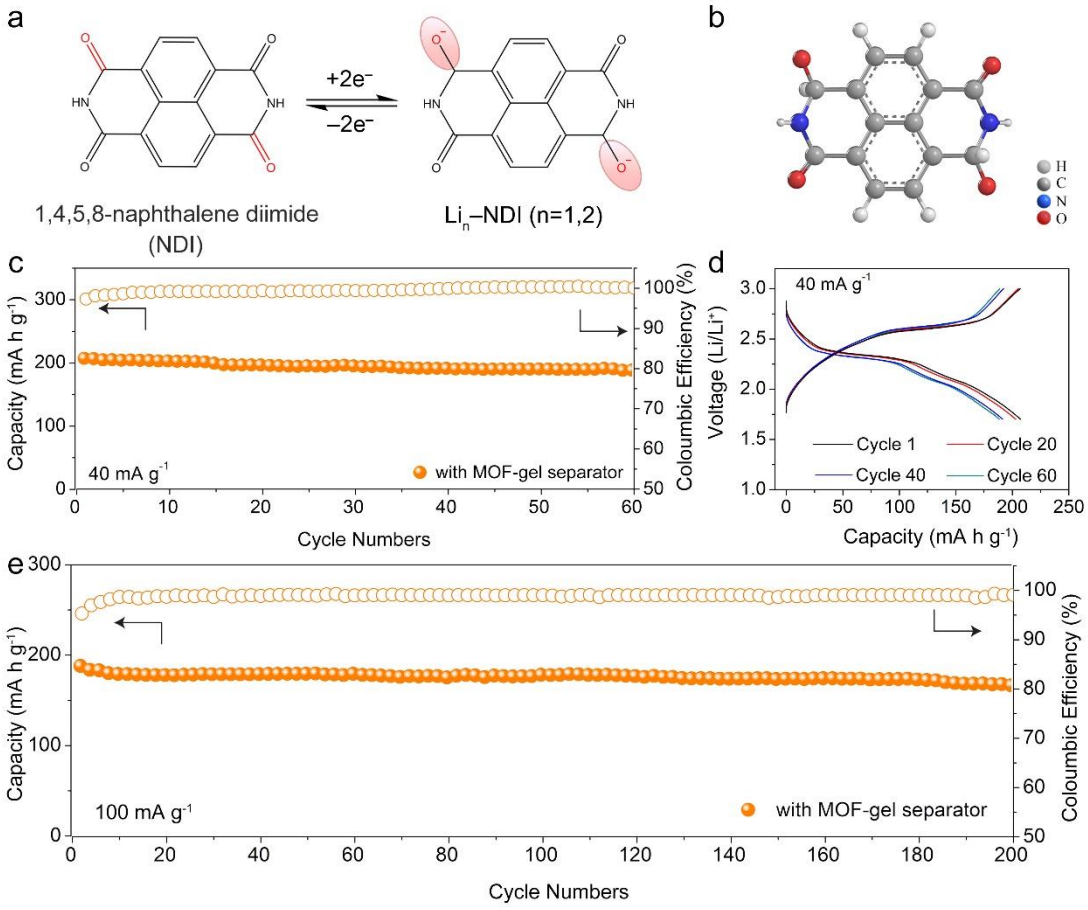

Supplementary Figure 25| Electrochemical performance of Li-NDI batteries. a, The proposed electrochemical redox reaction. **b,** The structures of Li_2-NDI intermediates. **c,** Cycling performance and coulombic efficiency for a current density of 40 mA g^{-1} for 60 cycles with MOF-gel separator. The capacity retention was 85% after 60 cycles. **d,** Discharge/charge voltage profiles at a current density of 40 mA g^{-1} with MOF-gel separator. **e,** Extended cycling performance and coulombic efficiency at a current density of 100 mA g^{-1} over 200 cycles.

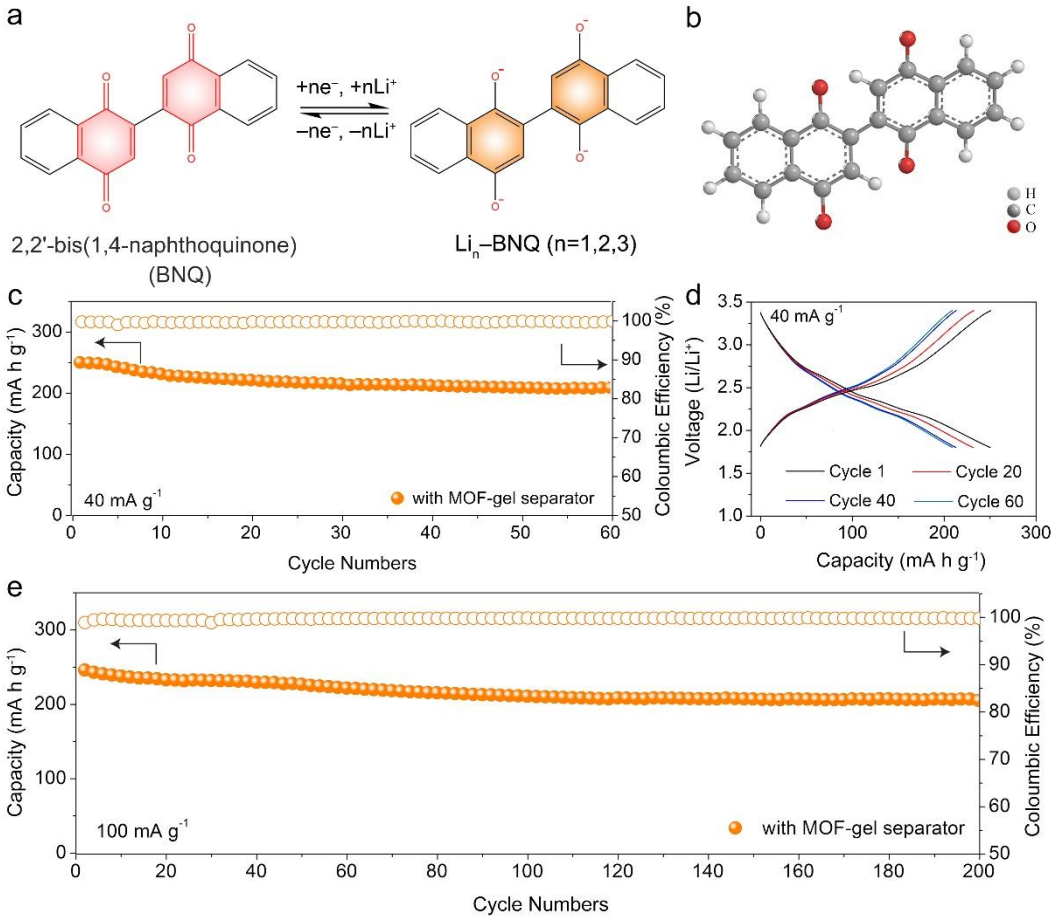

Supplementary Figure 26| Electrochemical performance of Li-BNQ batteries. a, The proposed electrochemical redox reaction. **b,** The structures of Li_3-BNQ intermediates. **c,** Cycling performance and coulombic efficiency for a current density of 40 mA g^{-1} over 60 cycles with MOF-gel separator. The capacity retention was 84% after 60 cycles. **d,** Discharge/charge voltage profiles at a current density of 40 mA g^{-1} with MOF-gel separator. **e,** Extended cycling performance and coulombic efficiency at a current density of 100 mA g^{-1} over 200 cycles.

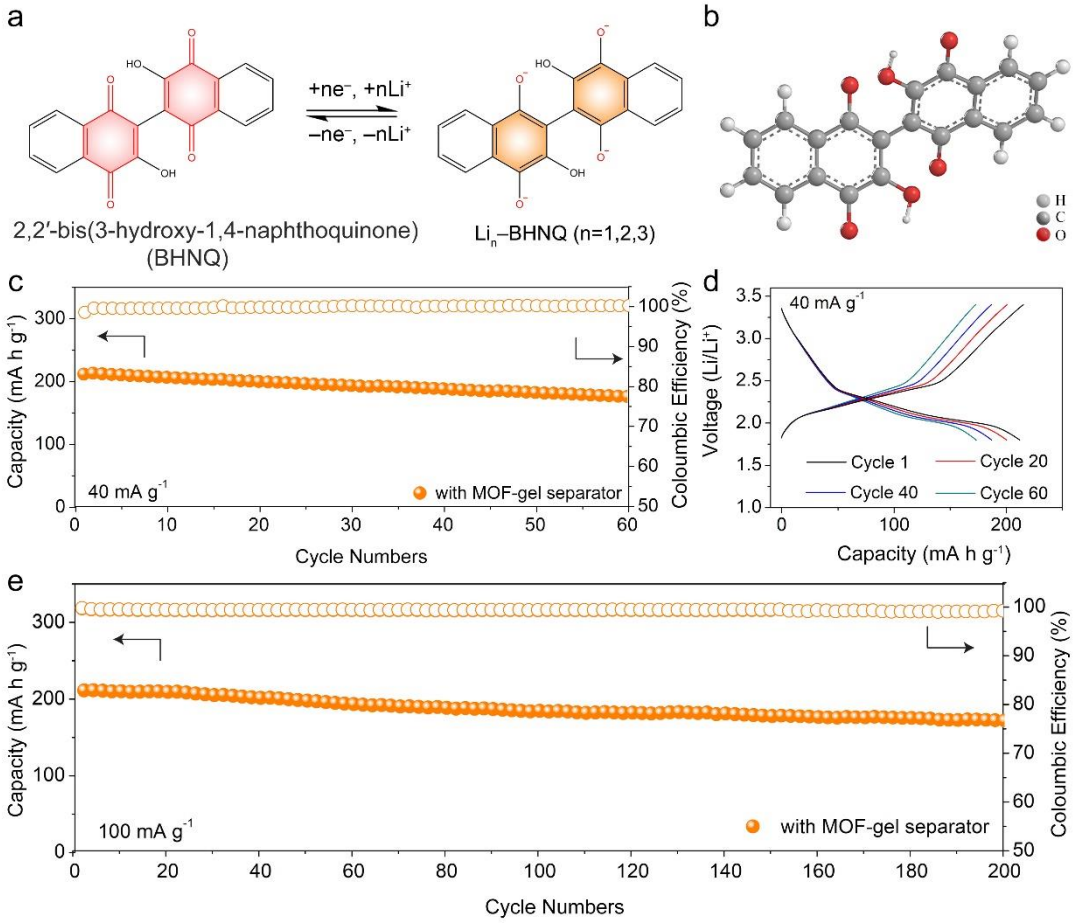

Supplementary Figure 27| Electrochemical performance of Li-BHNQ batteries. a, The proposed electrochemical redox reaction. **b,** The structures of Li_3-BHNQ intermediates. **c,** Cycling performance and coulombic efficiency for a current density of 40 mA g^{-1} for 60 cycles with MOF-gel separator. The capacity retention was 83% after 60 cycles. **d,** Discharge/charge voltage profiles at a current density of 40 mA g^{-1} with MOF-gel separator. **e,** Extended cycling performance and coulombic efficiency at a current density of 100 mA g^{-1} over 200 cycles.

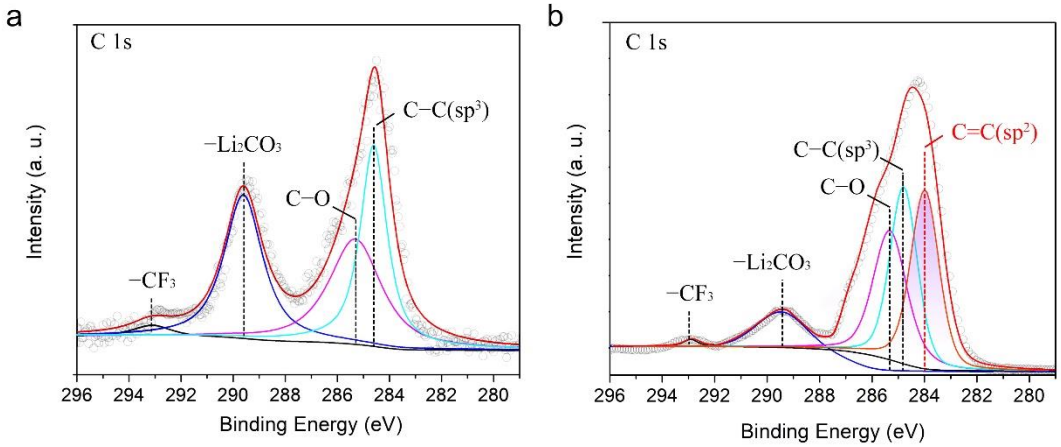

Supplementary Figure 28| XPS characterization of the passivation layer formed on the surface of Li-metal anode after 100 cycles at the current density of 30 mA g^{-1} with **a**, MOF-gel separator and **b**, Celgard separator. The obtained spectra (red lines) were deconvoluted by the XPS Peak 41 program. Since the presence of Me_2BBQ or its decomposed product would contain similar elements to that of the conventional SEI layer such as C and O, which makes its detection difficult based on the elemental analysis of the passivation layer; we rather focused on the difference on the bonding nature of C to verify the contribution of Me_2BBQ to the passivation layer, considering that Me_2BBQ contains a significant portion of the C = C double bond (sp^2 carbon), which is absent in ether-based electrolyte. This figure compares the C1s XPS spectra observed for the surface layer of lithium metal anodes from cells with **a,** MOF-gel separator and **b,** conventional Celgard separator after 100 cycles. **a** indicates that the observed peaks are attributable to the decomposed products of electrolyte solvents or Li salts, and no apparent peak related with the C = C double bond (sp^2 carbon) at 284.0 eV was detected for the lithium metal with the MOF-gel separator. On the other hand, the XPS peak at around 284.0 eV is significantly broad and asymmetric in the case of the conventional Celgard separator, and its peak deconvolution reveals that a substantial portion of C = C double bond is present. Moreover, due to the rise of the C = C double bond peak, the relative intensity of other peaks from Li_2CO_3 and CF_3 gets comparatively smaller. It is consistent with the SEM results, which depicted a thicker passivation layer for the lithium metal with the conventional Celgard separator, demonstrating the sieving roles of MOF-gel separator further.

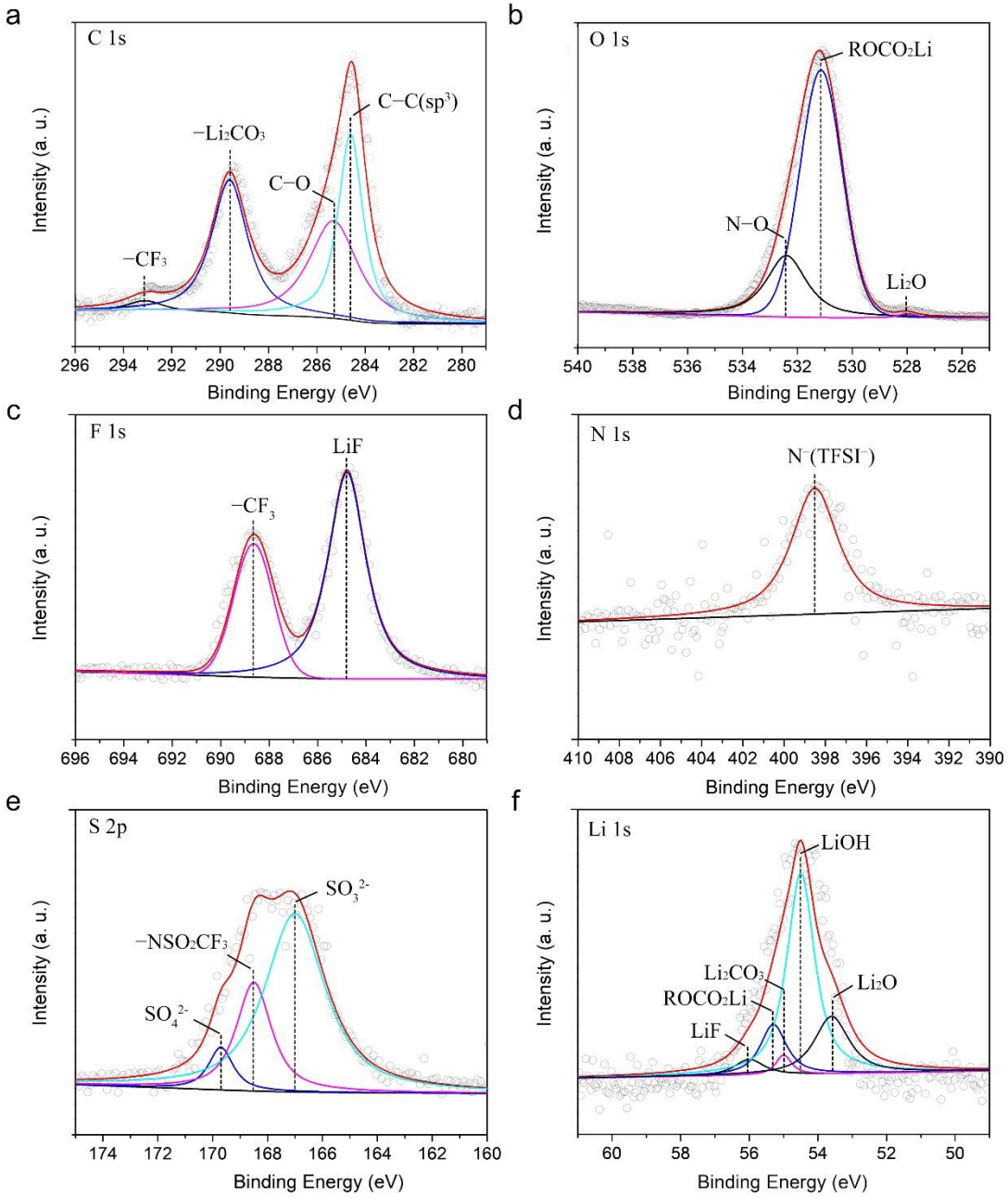

Supplementary Figure 29| XPS characterization of the passivation layer formed on the surface of Li-metal anode with MOF-gel separator after 100 cycles at the current density of 30 mA g^{-1}. Elemental spectra of **a,** C 1s, **b,** O 1s, **c,** F 1s, **d,** N 1s, **e,** S 2p and **f,** Li 1s are presented. The obtained spectra (red lines) were deconvoluted by using the XPS Peak 41 program. Each peak in these spectra is attributable to the presence of decomposed products of electrolyte solvents (C-O, C-C bond, $ROCO_2Li$, Li_2CO_3, Li_2O, and LiOH) or Li salts (-CF_3, N-O bond, LiF, N^-, SO_3^{2-}, SO_4^{2-}, and -NSO_2CF_3).

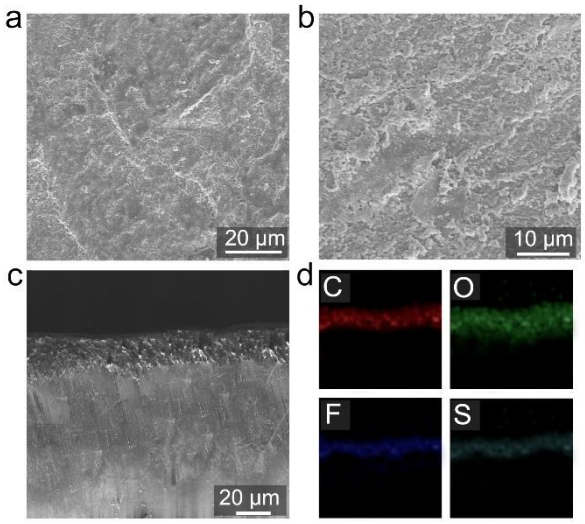

Supplementary Figure 30| a, b, Top-view SEM images and **c,** Cross-section SEM image of Li-metal electrode with MOF-gel separator at current density of 300 mA cm^{-2} after 1000 cycles. **d,** EDS elemental mapping images of cycled Li-metal electrode with MOF-gel separator.

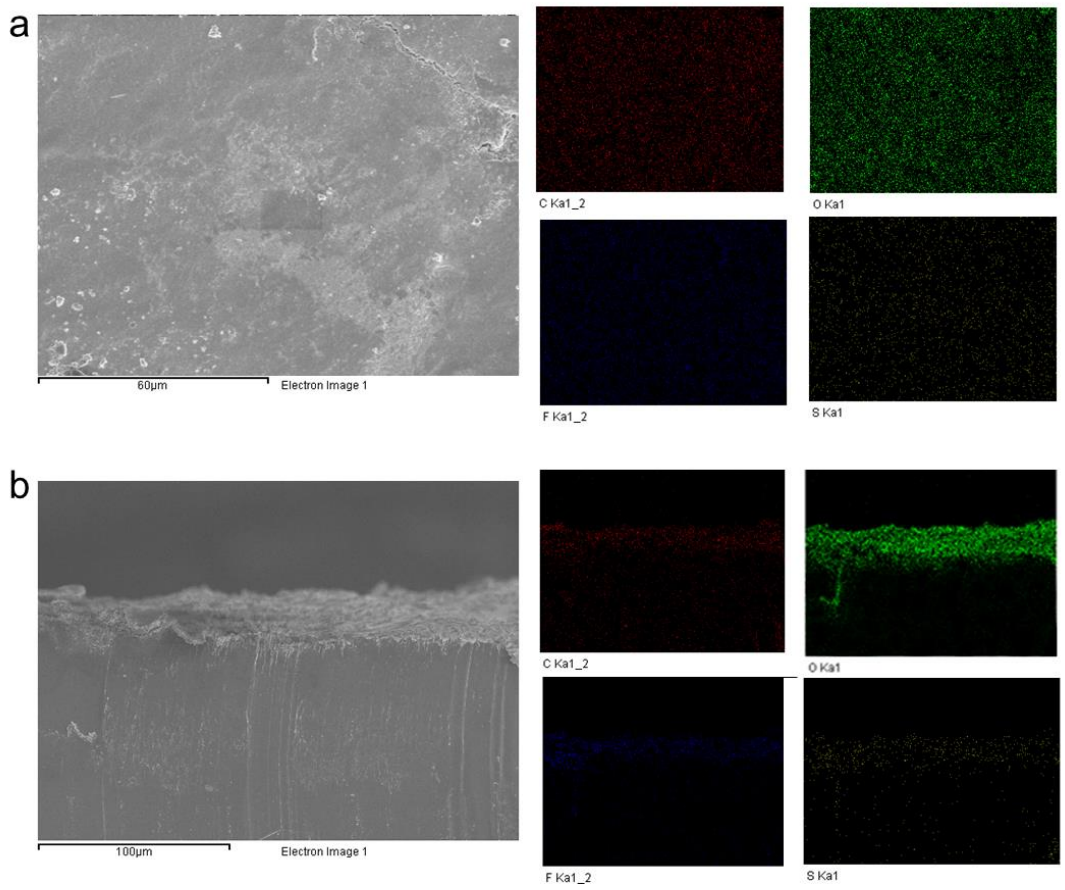

Supplementary Figure 31| The morphologies and EDS spectra of the lithium metal anode in Li-AQ battery with a MOF-gel separator along **a,** the top-view and **b**, cross-section. The Li-AQ battery with a MOF-gel separator was cycled over 100 cycles. A relatively uniform passivation layer with a thickness of ~20 µm was formed on the Li-metal electrode retrieved from the cell with the MOF-gel separator, whereas a significantly roughened surface with a coarsely packed passivation layer of ~70-µm-thickness was observed for the reference cell (Supplementary Fig. 32). The EDS elemental mappings show a well-protected passivation layer (~ 20 µm thickness) on top of the lithium-metal anode.

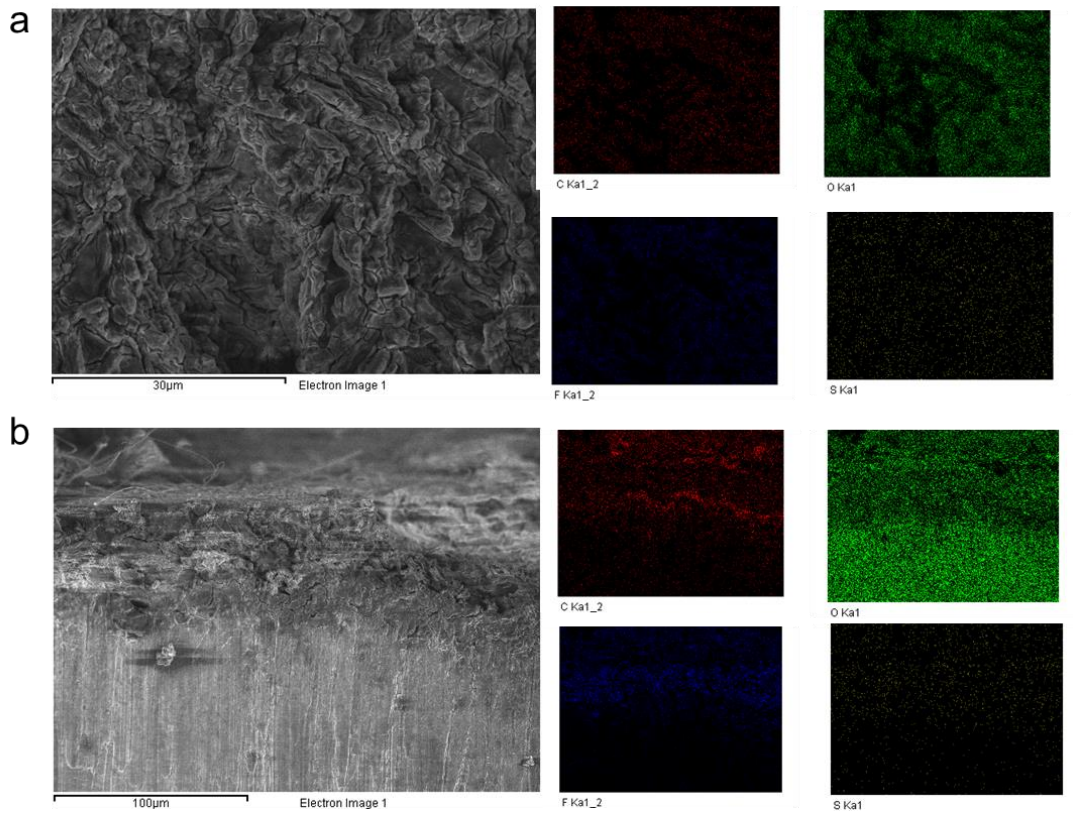

Supplementary Figure 32| The morphologies and EDS spectra of the lithium metal anode in Li-AQ battery with a Celgard separator along **a,** the top-view and **b,** cross-section. The Li-AQ battery with a Celgard separator was cycled over 50 cycles. The EDS elemental mappings show a well-protected passivation layer (~ 70 µm thickness) on top of the lithium-metal anode.

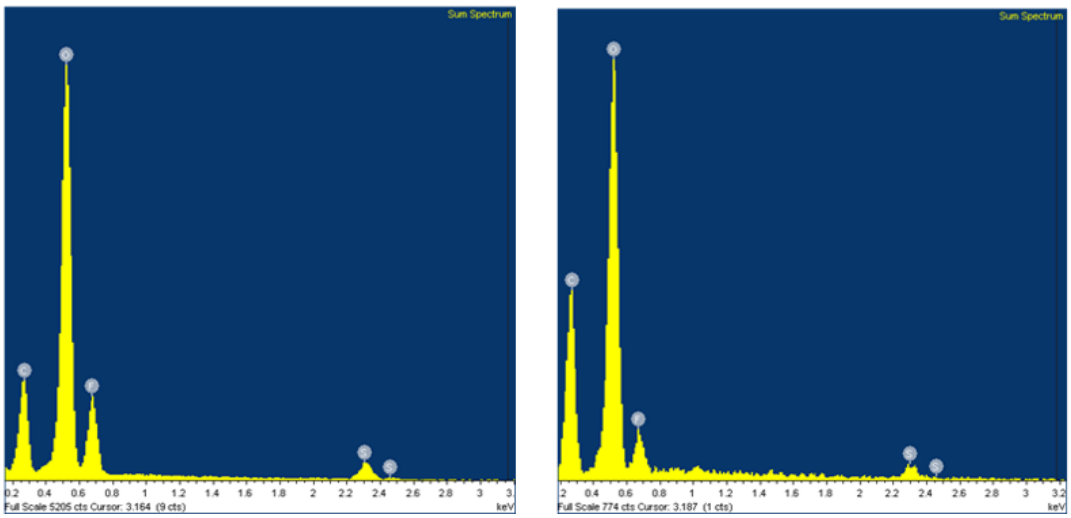

Supplementary Figure 33| The EDS spectra with no Zn signals on the cycled lithium metal anode. Li–Me_2BBQ battery with a MOF-gel separator was cycled over 100 cycles.

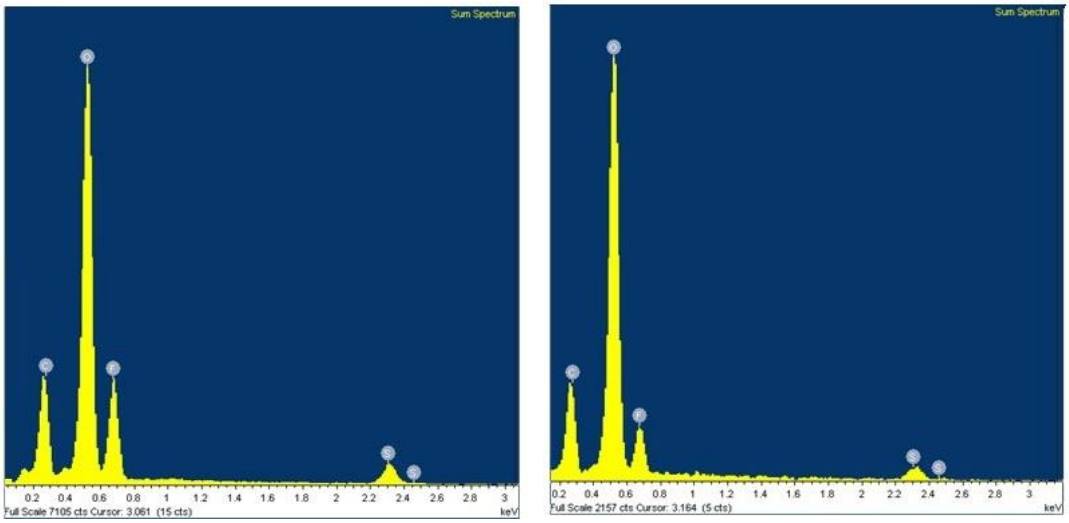

Supplementary Figure 34| The EDS spectra with no obvious Zn signals on the cycled lithium metal anode. The Li-AQ battery with a MOF-gel separator was cycled over 100 cycles.

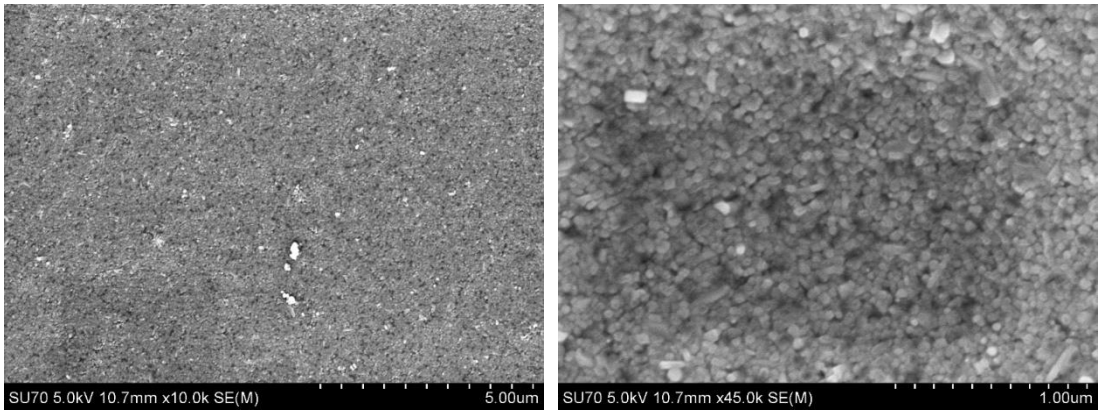

Supplementary Figure 35| Morphologies of the cycled MOF-gel separator. **a,** SEM images of MOF-gel separator after 200th discharge/charge cycles. **b,** The enlarged SEM images.

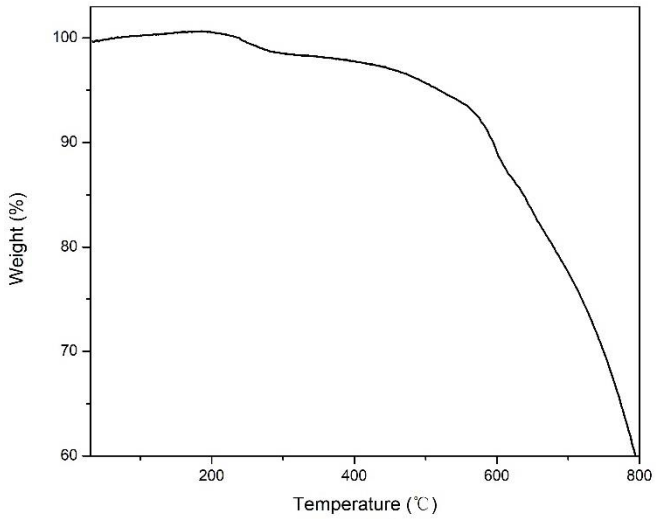

Supplementary Figure 36| The thermal stability of MOF-gel separator.

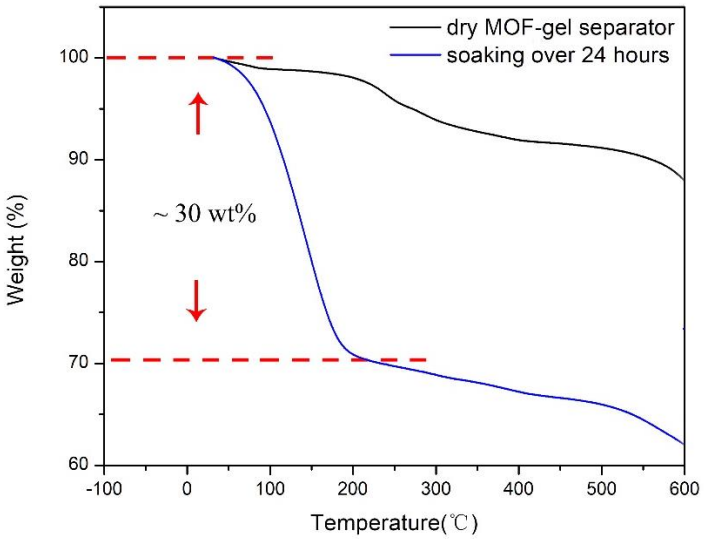

Supplementary Figure 37| Thermogravimetric analysis. The electrolyte content of MOF-gel separator after soaking in electrolyte is indicated.

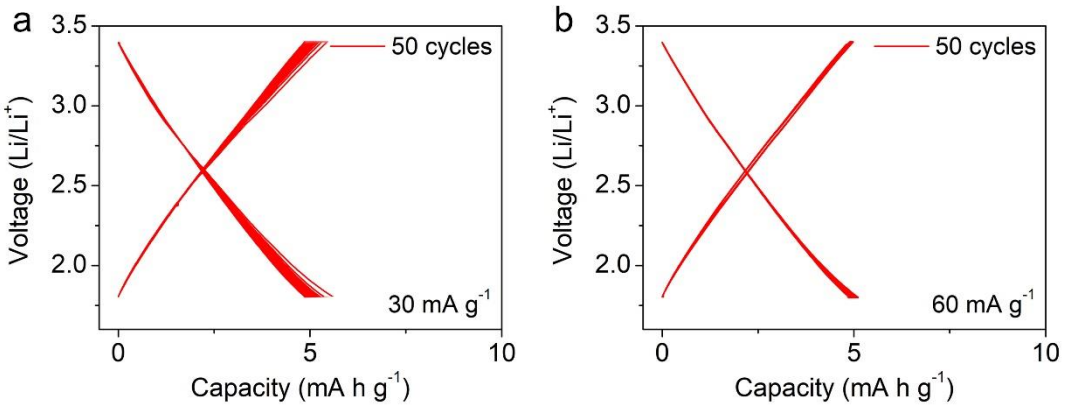

Supplementary Figure 38 | Electrochemical tests showing the contribution of Super P to the capacity. They were measured in the voltage range of 1.8–3.4 V (versus Li^+/Li) and at the current density of **a,** 30 mA g^{-1} and **b,** 60 mA g^{-1}. The capacity derived from Super P is only ~5 mA h g^{-1} for both cases.

Synthetic procedures:

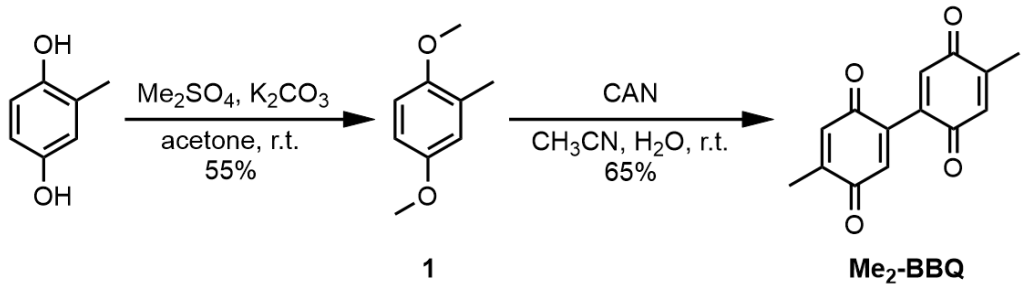

Supplementary Figure 39| The synthetic route of Me_2BBQ.

2,5-Dimethoxytoluene (**1**). The compound was synthesized following a slightly modified literature procedure[1]. A 100 mL round-bottom-flask was loaded with methylhydroquinone (1.25 g, 10.1 mmol), K_2CO_3 (5.54 g, 40.1 mmol), and acetone (45 mL). With stirring at room temperature, Me_2SO_4 (2.4 mL, 25.3 mmol) was added. The reaction mixture was stirred while heated to reflux for 15 hours, and poured into water (100 mL). The organic fraction was extracted with dichloromethane (2×100 mL), dried over anhydrous $MgSO_4$, filtered, and concentrated under reduced pressure. Resulting colorless liquid was purified by flash column chromatography on SiO_2 (hexanes:dichloromethane = 1:1, v/v) to furnish **1** as a colorless liquid (0.840 g, 5.52 mmol, yield = 55%). ^{1}H NMR (500 MHz, $CDCl_3$, 298 K): δ 6.77–6.71 (m, 2H), 6.71–6.65 (m, 1H), 3.78 (s, 3H), 3.76 (s, 3H), 2.21 (s, 3H). ^{13}C NMR (125 MHz, $CDCl_3$, 298 K): δ 153.6, 152.3, 128.0, 117.2, 111.2, 111.0, 56.1, 55.9, 16.5. FT-IR (ATR, cm^{-1}): 2996, 2946, 2832, 1499, 1465, 1419, 1280, 1220, 1180, 1157, 1130, 1048, 1031, 795, 752.

4,4'-dimethyl-1,1'-bi(cyclohexa-3,6-diene)-2,2',5,5'-tetraone (**Me_2BBQ**). The compound was synthesized following a literature procedure[2]. A 50 mL round-bottom flask was loaded with **1** (87.7 mg, 0.576 mmol), and MeCN (2 mL). When stirring at room temperature, aqueous solution (2 mL) of ceric ammonium nitrate (1.16 g, 2.12 mmol) was added dropwise. The reaction mixture was kept stirring at room temperature for 1 hour, and poured into water (15 mL). The resulting precipitate was collected by filtration, and dried under an air stream. Recrystallization from *ca*. 6 mL of boiling mixture of ethanol and chloroform (1:1, v/v) furnished **Me_2BBQ** as a yellow crystal (45.2 mg, 0.187 mmol, yield = 65%). ^{1}H NMR (500 MHz, $CDCl_3$, 298 K): δ 6.81 (s, 2H), 6.70 (q, J = 1.6 Hz, 2H), 2.10 (d, J = 1.6 Hz, 2H). ^{13}C NMR (125 MHz, $CDCl_3$, 298 K): δ 187.1, 184.9, 146.4, 139.7, 136.1, 133.8, 15.7. FT-IR (ATR, cm^{-1}): 1646, 1627, 1575, 1433, 1355, 1323, 1233, 1203, 1122, 1034, 1009, 927, 911, 883, 782, 715.

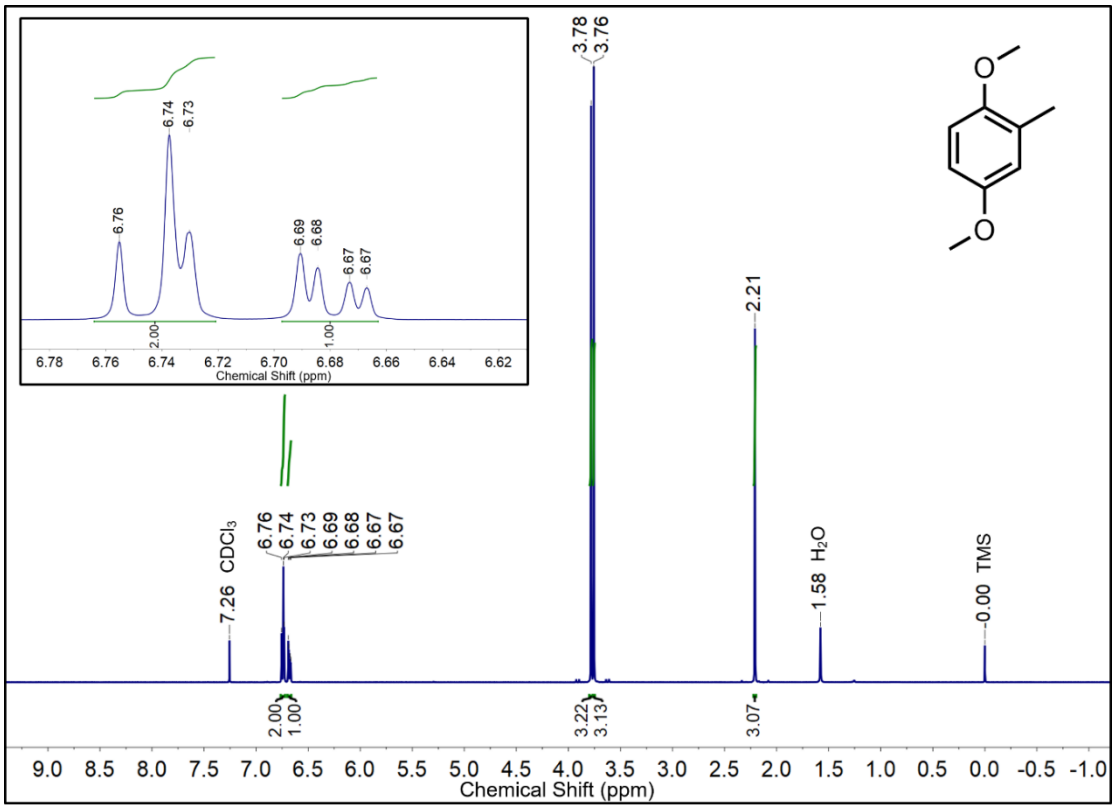

Supplementary Figure 40| ^{1}H NMR (500 MHz) spectrum of **1** in $CDCl_3$ (T = 298 K).

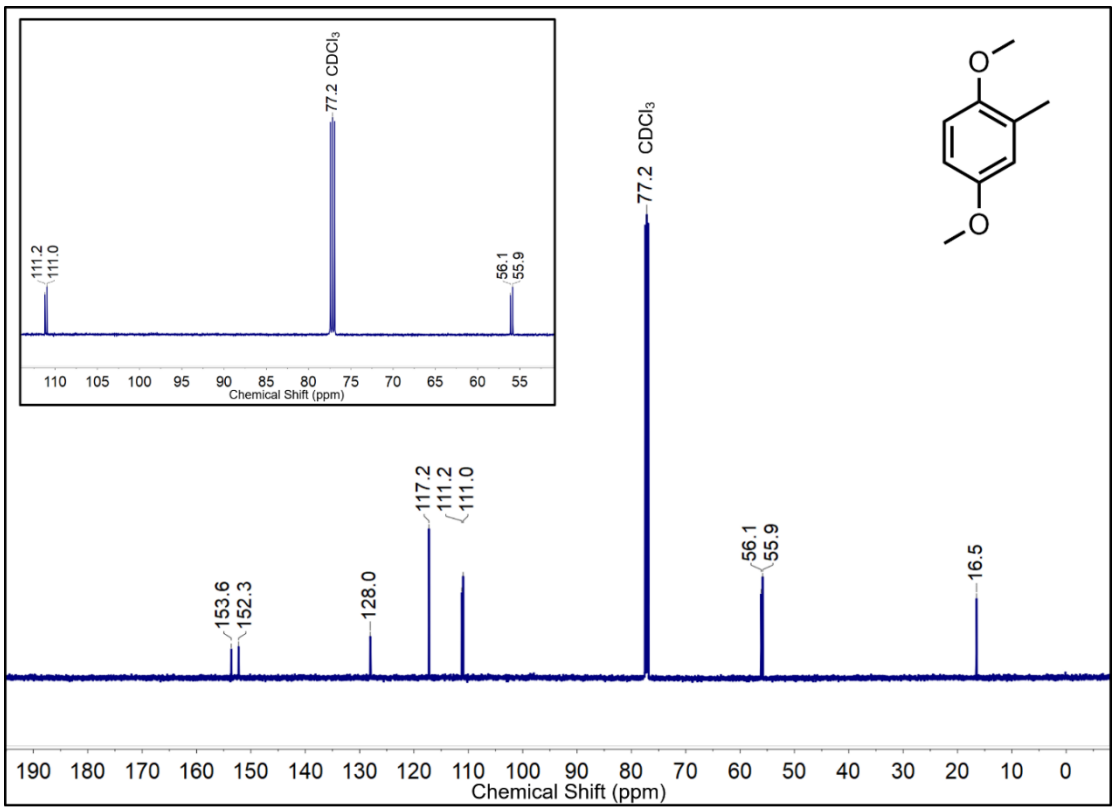

Supplementary Figure 41| ^{13}C NMR (125 MHz) spectrum of **1** in $CDCl_3$ (T = 298 K).

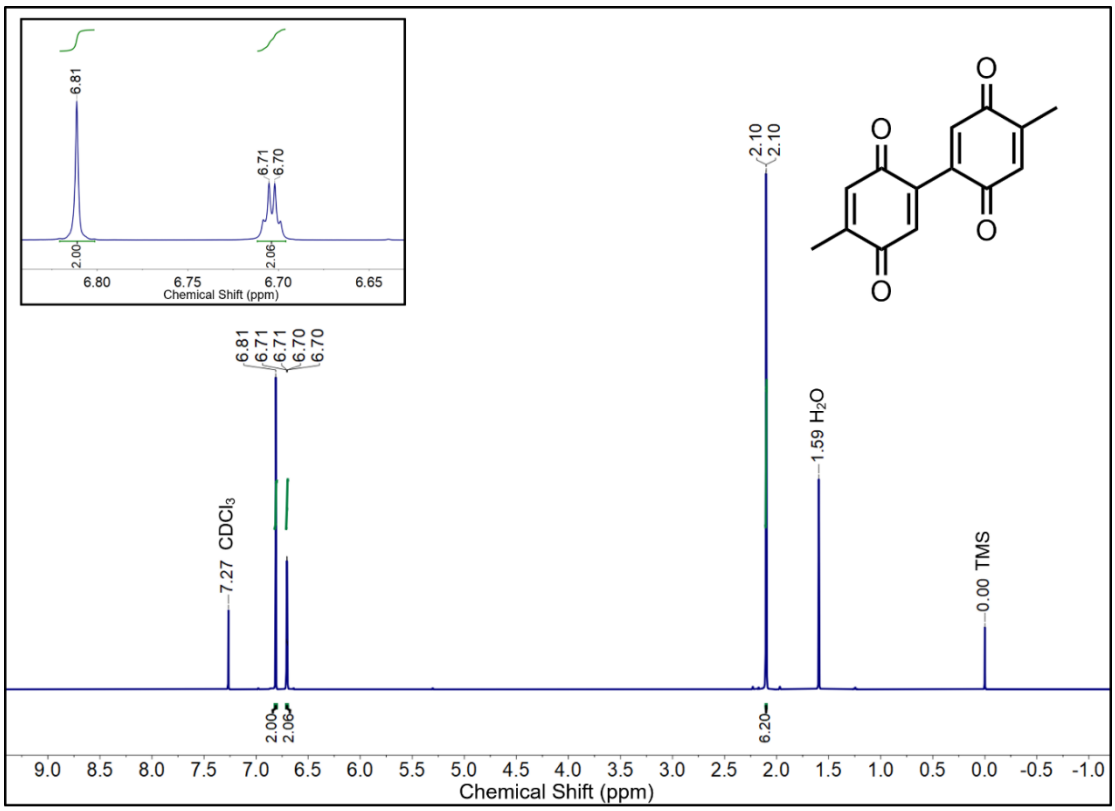

Supplementary Figure 42| ^{1}H NMR (500 MHz) spectrum of **Me_2BBQ** in $CDCl_3$ (T = 298 K).

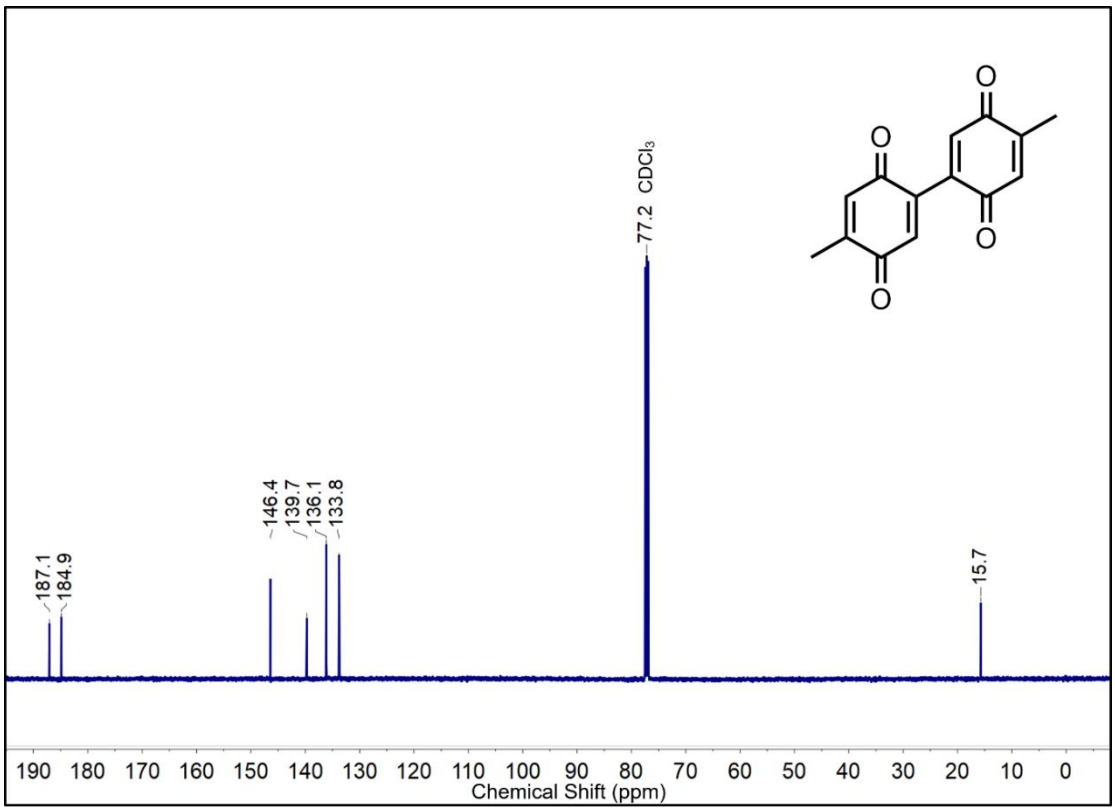

Supplementary Figure 43| ^{13}C NMR (125 MHz) spectrum of **Me_2BBQ** in $CDCl_3$ (T = 298 K).

Supplementary Note

Supplementary Note 1. The strain-stress performance.

To evaluate the mechanical properties of the MOF-gel separator, we examined the elastic modulus (E) and hardness (H) using the nanoindentation method. The strain-stress equation can be described as follows:

$$\mathrm{E}_r = \left(\frac{1-\nu^2}{E} + \frac{1-{\nu_i}^2}{E_i}\right)^{-1} \qquad (1)$$

, where E_r is the Elastic modulus and ν is the Poisson's ratio of the specimen, while E_i is the Elastic modulus of the indenter tip (1140 GPa) and ν_i is the Poisson's ratio of the indenter tip (0.07). The elastic modulus (E) and hardness (H) were obtained from a series of indentation experiments as a function of the indentation depth on a monolithic MOF-gel separator, as depicted in Supplementary Fig. 8. In this process, averaged properties were derived from 100 indents by using penetration depths up to 600nm. The average E and H values of our MOF-gel separator were calculated to be 4.16 ± 0.577 GPa and 0.414 ± 0.0963 GPa, respectively. These values are comparable or slightly higher than those reported for conventional separators and other MOF-based membranes separators[3-8]. In Supplementary Table 1, we compared the E and H values of MOF-gel separator with those previously reported for conventional functional separators in lithium-ion batteries. It is also noteworthy that the elastic modulus of our MOF-gel separator is much higher than that of conventional polymer matrix membrane, and even higher than that of pristine ZIF-8 particles. It is attributed to the gelation process retaining the gel macrostructures and overcoming the intrinsic defects of MOF particles, and forming a dense and monolithic ZIF-8 xerogel. The MOF-gel separator indicated its good mechanical durability against permanent plastic deformation. The high mechanical strength of the monolithic MOF-gel separator would also lead to a mechanical reliability, giving rising to potential benefits potentials in practical applications.

Supplementary Table 1 | Comparisons of the stress-strain properties.

Sample name	*Elastic modulus (GPa)*	*Hardness (GPa)*	*References*
PVDF separator	0.0389	0.00325	*J Power Sources*; (240); 204-211
Celgard® separator (2325)	0.3444	0.0109	*J Power Sources*; (348); 255-263
Celgard® separator (2400)	0.43 ± 0.023	0.0142 ± 0.004	*J Power Sources*; (196); 8728-8734
PVA separators (polyvinyl alcohol)	0.278	0.0171	*J Mater Chem A*; 12(7); 6859-6868
ZIF-8/Matrimid®	2.2 ± 0.1	0.0476 ±0.0033	*J Membrane Sci*;

MMMs (60 wt% ZIF-8)			1-2(361); 28-37
conventional ZIF-8 particles	3.3	0.5	*P Natl Acad Sci*; 22(107); 9938-9943
MOF-gel separator (ZIF-8)	4.16 ± 0.577	0.414 ± 0.0963	This work

Supplementary Note 2. Calculation of Li^+ ion conductivity

We measured the ion conductivity and the activation energy following the conventional protocol of the ionic-conductivity measurement for Celgard and the MOF-gel separators. Cells were prepared by inserting pristine Celgard 2400 separators or the MOF-gel separators between two stainless steel electrodes and by employing the electrolyte of 1 M lithium bis(trifluoromethanesulfonyl)imide (LiTFSI) dissolved in a mixture of 1,3-dioxolane (DOL) and dimethoxyethane (DME).

Ionic conductivity measurements were performed by electrical impedance spectroscopy (EIS) according the equation (2):

$$\sigma = L \times S^{-1} \times R^{-1} \qquad (2)$$

where σ is the ion conductivity, L is the distance between the two stainless steel electrodes, while the S is the geometric area of electrode/electrolyte interface and the R is the intercept at the real axis in the impedance Nyqiusit plot. Impedance spectra and corresponding ion conductivity values are presented in Supplementary Fig. 20.

Lithium-ion diffusion through the MOF-gel separator during the permeation measurements (Me_2BBQ^{n-} permeation in Supplementary Fig. 14 and BQ^{n-} permeation in Supplementary Fig. 16) was also observed, and the results are presented in Supplementary Table 2, 3. After BQ^{n-} permeation for over 36 hours, the Li^+ ionic conductivity was determined to be ~2.8 and ~2.7 mS cm^{-1} for the outer and inner cylinder, respectively, indicating the transport of lithium ions. Similar behaviours were also observed for the Me_2BBQ^{n-} permeation experiment. A significant amount of lithium ions was detected in the outer-cylinder solution, with the inner and outer cylinder electrolytes exhibiting identical ionic conductivities of ~2.7 mS cm^{-1}, confirming the transport of lithium ions though the MOF-gel separator. Although, at the same temperature, the Li^+ ionic conductivity with the MOF-gel separator is lower than that with conventional Celgard separators (see Supplementary Fig. 20), it is still comparable to what have been reported for other functional separators[9, 10].

Supplementary Table 2 | Comparisons of the Li^+ ionic conductivity before and after permeation experiments of BQ^{n-} at ambient temperature. The conductivity of fully-discharged BQ^{2-} intermediates dissolved in electrolyte (1M LiTFSI in DOL/DME) was measured as 7.8 mS cm^{-1}. The Li^+ ionic conductivities were estimated as ~2.8 mS cm^{-1} (outer cylinder) and ~2.7 mS cm^{-1} (inner cylinder).

Before Permeation	Li^+ ionic conductivity (mS cm^{-1})	After Permeation	Li^+ ionic conductivity (mS cm^{-1})
BQ^{2-} Solution (Inner)	7.8	Mixed Solution (Inner)	2.7
Blank DOL/DME mixture	-	Mixed Solution (outer)	2.8

Supplementary Table 3 | Comparisons of the Li^+ ionic conductivity before and after permeation experiments of $MeBBQ^{n-}$ at ambient temperature. Ionic conductivities were measured following the protocols specified in Supplementary Note 2. In the permeation device with Me_2BBQ^{n-} solution, the inner cylinder and the outher cylinder exhibit the same Li^+ conductivity of 2.7 mS cm^{-1}, demonstrating the facile Li^+ conduction through the MOF-gel separator.

Before Permeation	Li^+ ionic conductivity (mS cm^{-1})	After Permeation	Li^+ ionic conductivity (mS cm^{-1})
Me_2BBQ^{n-} Solution (Inner)	7.6	Mixed Solution (Inner)	2.7
Blank DOL/DME mixture	-	Mixed Solution (outer)	2.7

For the situation that the liquid electrolyte is the actual media into which the Li^+ diffuses, the MOF-gel separator behaves like a porous matrix for its size effects, which is in preferable agreement with the Vogel–Tamman–Fulcher (VTF) equation (3). As listed below, the relationship of the VTF behaviour, which can be well described:

$$\sigma = \sigma_0 T^{-1/2} \exp\left(-\frac{E_a}{R(T - T_0)}\right) \qquad (3)$$

where σ is the conductivity, σ_0 is the pre-exponential factor, while E_a is a pseudo activation energy, T the absolute temperature, T_0 is the glass transition temperature, and R is the ideal gas constant. Following the VTF equation, E_a was calculated based on the experimental data. Moreover, according to the Arrhenius plot, the plots of $\ln(\sigma T^{1/2})$ versus $(T\text{-}T_0)^{-1}$ exhibit a linear relationship. From those process, we calculated the activation energy for the Li^+ ion conduction. A least-square-fitting regression on the experimental data revealed that the activation barrier for the system with Celgard separator is about 0.1 eV. On the other hand, the activation barrier for the cell employing the MOF-gel separator was calculated to be higher with approximately 0.78 eV. Along with the comparatively lower ionic conductivity measured above, it indicates that the general ionic transport property is not as good as that of the conventional Celgard separators, and some degree of

compromise of lithium-ion conductivity is inevitable in MOF-gel separator. Nevertheless, compared with other common separators, the calculated activation energy still locates at a rational level, similar to values from a series of researches reported[9, 10].

Supplementary Table 4 | Active material loading of each sample in Fig. 2 (i~viii points) before and after dissolution tests.

	Mass loading (mg cm^{-2})		Weight changes
	As-prepared	After dissolution	
Sample i	0.499	0.498	0.2
Sample ii	0.49	0.334	31.8 %
Sample iii	0.492	0.1565	68.2 %
Sample iv	0.491	0.00589	98.8 %
Sample v	0.49	0.122	75.1 %
Sample vi	0.493	0.302	38.7 %
Sample vii	0.495	0.412	16.8 %
Sample viii	0.497	0.468	5.8 %

References

1 Mehta, G., Khan, T. B. & Kumar, Y. C. S. Total synthesis of the fungal metabolite (+/-)-acremine G: acceleration of a biomimetic Diels-Alder reaction on silica gel. *Tetrahedron Lett* **51**, 5116-5119 (2010).

2 Yokoji, T., Kameyama, Y., Maruyama, N. & Matsubara, H. High-capacity organic cathode active materials of 2,2'-bis-p-benzoquinone derivatives for rechargeable batteries. *J Mater Chem A* **4**, 5457-5466, (2016).

3. Liang Y*, et al.* Heat treatment of electrospun Polyvinylidene fluoride fibrous membrane separators for rechargeable lithium-ion batteries. *J Power Sources* **240**, 204-211 (2013).

4. Kalnaus S, Wang Y, Turner JA. Mechanical behavior and failure mechanisms of Li-ion battery separators. *J Power Sources* **348**, 255-263 (2017).

5. Sheidaei A, Xiao X, Huang X, Hitt J. Mechanical behavior of a battery separator in electrolyte solutions. *J Power Sources* **196**, 8728-8734 (2011).

6. Wang W*, et al.* A 3D flexible and robust HAPs/PVA separator prepared by a freezing-drying method for safe lithium metal batteries. *J Mater Chem A* **7**, 6859-6868 (2019).

7. Ordoñez MJC, Balkus KJ, Ferraris JP, Musselman IH. Molecular sieving realized with ZIF-8/Matrimid® mixed-matrix membranes. *J Membrane Sci* **361**, 28-37 (2010).

8. Tan JC, Bennett TD, Cheetham AK. Chemical structure, network topology, and porosity effects on the mechanical properties of Zeolitic Imidazolate Frameworks. *Proceedings of the National Academy of Sciences* **107**, 9938-9943 (2010).

9. Bai S, Liu X, Zhu K, Wu S, Zhou H. Metal–organic framework-based separator for lithium–sulfur batteries. *Nature Energy* **1**, 16094 (2016).

10. Schon TB, McAllister BT, Li P-F, Seferos DS. The rise of organic electrode materials for energy storage. *Chem Soc Rev* 2016, **45**(22)**:** 6345-6404.